

Water Resources Research

RESEARCH ARTICLE

10.1029/2019WR026635

Signatures of Hydrologic Function Across the Critical Zone Observatory Network



Key Points:

- Quantitative signatures of hydrologic function show variations across the U.S. Critical Zone Observatory network
- Dynamic water storage range is correlated with hydroclimatic seasonality of water inputs
- Variations in catchment sensitivity and baseflow index point toward underlying structural controls

Supporting Information:

- Supporting Information S1
- Data Set S1

Correspondence to:

A. N. Wlostowski,
awlostowski@lynkertech.com

Citation:

Wlostowski, A. N., Molotch, N., Anderson, S. P., Brantley, S. L., Chorover, J., Dralle, D., et al. (2021). Signatures of hydrologic function across the Critical Zone Observatory network. *Water Resources Research*, 57, e2019WR026635. <https://doi.org/10.1029/2019WR026635>

Received 28 OCT 2019

Accepted 7 OCT 2020

Accepted article online 18 OCT 2020

Adam N. Wlostowski^{1,2} , Noah Molotch^{2,3} , Suzanne P. Anderson^{2,4} , Susan L. Brantley⁵ , Jon Chorover⁶ , David Dralle^{7,8} , Praveen Kumar⁹ , Li Li¹⁰ , Kathleen A. Lohse¹¹ , John M. Mallard¹² , Jennifer C. McIntosh⁶ , Sheila F. Murphy¹³ , Eric Parrish², Mohammad Safeeq^{14,15} , Mark Seyfried¹⁶ , Yuning Shi¹⁷ , and Ciaran Harman^{18,19} 

¹Lynker Technologies, LLC, Boulder, CO, USA, ²Institute of Arctic and Alpine Research, University of Colorado Boulder, Boulder, CO, USA, ³Department of Geography, University of Colorado Boulder, Boulder, CO, USA, ⁴Department of Geological Sciences, University of Colorado Boulder, Boulder, CO, USA, ⁵Earth and Environmental Systems Institute and Department of Geosciences, Pennsylvania State University, University Park, PA, USA, ⁶Department of Hydrology and Atmospheric Sciences, University of Arizona, Tucson, AZ, USA, ⁷Department of Earth and Planetary Science, University of California Berkeley, Berkeley, CA, USA, ⁸Pacific Southwest Research Station, US Forest Service, Davis, CA, USA, ⁹Department of Civil and Environmental Engineering, University of Illinois, Urbana, IL, USA, ¹⁰Department of Civil and Environmental Engineering, Pennsylvania State University, University Park, PA, USA, ¹¹Department of Geosciences, Idaho State University, Pocatello, ID, USA, ¹²Nicholas School of the Environment, Duke University, Durham, NC, USA, ¹³U.S. Geological Survey, Boulder, CO, USA, ¹⁴Sierra Nevada Research Institute, University of California, Merced, CA, USA, ¹⁵Pacific Southwest Research Station, United States Forest Service, Fresno, CA, USA, ¹⁶Northwest Watershed Research Center, Agricultural Research Service, United States Department of Agriculture, Boise, ID, USA, ¹⁷Department of Ecosystem Science and Management, Pennsylvania State University, University Park, PA, USA, ¹⁸Department of Environmental Health and Engineering, Johns Hopkins University, Baltimore, MD, USA, ¹⁹Department of Earth and Planetary Sciences, Johns Hopkins University, Baltimore, MD, USA

Abstract Despite a multitude of small catchment studies, we lack a deep understanding of how variations in critical zone architecture lead to variations in hydrologic states and fluxes. This study characterizes hydrologic dynamics of 15 catchments of the U.S. Critical Zone Observatory (CZO) network where we hypothesized that our understanding of subsurface structure would illuminate patterns of hydrologic partitioning. The CZOs collect data sets that characterize the physical, chemical, and biological architecture of the subsurface, while also monitoring hydrologic fluxes such as streamflow, precipitation, and evapotranspiration. For the first time, we collate time series of hydrologic variables across the CZO network and begin the process of examining hydrologic signatures across sites. We find that catchments with low baseflow indices and high runoff sensitivity to storage receive most of their precipitation as rain and contain clay-rich regolith profiles, prominent argillic horizons, and/or anthropogenic modifications. In contrast, sites with high baseflow indices and low runoff sensitivity to storage receive the majority of precipitation as snow and have more permeable regolith profiles. The seasonal variability of water balance components is a key control on the dynamic range of hydraulically connected water in the critical zone. These findings lead us to posit that water balance partitioning and streamflow hydraulics are linked through the coevolution of critical zone architecture but that much work remains to parse these controls out quantitatively.

1. Introduction

The U.S. Critical Zone Observatories (CZOs) were created to advance understanding of the thin layer of the Earth's surface extending from unweathered bedrock to the top of the vegetation canopy (Brantley et al., 2007; White et al., 2015). CZOs have focused the efforts of teams of scientists working across disciplines by collecting data sets that characterize the physical, chemical, and biological architecture of the critical zone and its fluxes (e.g., Brantley et al., 2016). CZOs are seeking to advance fundamental understanding of how processes interact within this thin epithelium of the Earth, particularly how these processes sustain life and react to changing climate, tectonic, and land use drivers.

The U.S. CZOs were not initially conceived as a network—each was initiated with its own set of science questions and research approaches. However, they offer a unique opportunity to develop a cross-site

©2020. The Authors.

This is an open access article under the terms of the Creative Commons Attribution License, which permits use, distribution and reproduction in any medium, provided the original work is properly cited.

synthesis of understanding gained in the first decade of CZO research. Scientific synthesis can promote the development of broader questions and transferable hypotheses about the interactions between water, rock, energy, and biota in the critical zone (Brooks et al., 2015). One such question at the core of this pursuit is the following: how do landscapes store and partition water? The CZOs provide observations that allow investigators to interrogate the relationship between critical zone structure and hydrologic response across a suite of geologically and climatically diverse sites. Using data from 15 CZO sites, this paper compares catchments based on hydrologic function (Black, 1997; Wagener et al., 2007)—the partitioning, storage, and release water. In doing so, this work documents initial patterns of hydrologic variability across CZO catchments, laying a foundation for future cross-site investigations.

The partitioning, storage, and transmission of water are central landscape functions with numerous direct interconnections to other critical zone processes, including those that support human societies (Black, 1997; Loomis et al., 2000; Poff et al., 1997; Wagener et al., 2008). For example, the quantity of water available for ecological, industrial, and municipal use depends on the partitioning of precipitation between evapotranspiration, runoff, and groundwater recharge (Bales et al., 2006, 2018). Similarly, the timing and quantity of runoff depend on the orientation of flow paths responsible for runoff generation (Jencso et al., 2010; Payn et al., 2012). The chemical quality of surface water and groundwater depends on the residence time and composition of hydrologic flow paths (Maher, 2011). Plant ecosystem structure and productivity depend on soil water storage (Eagleson, 1982; Graham et al., 2010). Hydrologically mediated landscape functions such as these are relevant over short timescales (days to decades) and largely depend on the interplay of climate and landscape architecture (i.e., soils, regolith, and topographic properties) (Field et al., 2015; Tague & Grant, 2009).

Over longer timescales (decades to millennia), water partitioning, storage, and transmission paces the evolution of landscapes. Water is a primary control on the spatial distribution and properties of soil and regolith (Jenny, 1941). The conversion of fresh bedrock to soil requires meteoric water to chemically and physically break down the rock (Brantley & Lebedeva, 2011; Maher, 2010; Rempe & Dietrich, 2014). Conversely, fluvial incision, itself affected by water transmission, affects the distribution of soil and regolith and the morphology of hillslopes (Deal et al., 2018). Hydrologic processes also modify soil and regolith drainage characteristics (Jefferson et al., 2010). For example, the development of subsurface clay horizons affects the orientation of flow paths by promoting the development of shallow, transient, and perched water tables (Lohse & Dietrich, 2005; Zimmer & McGlynn, 2017). Further, the development of reaction fronts in the subsurface may have strong control on the orientation of deeper flow paths contributing to baseflow (Brantley et al., 2017).

An underlying but implicit hypothesis of the CZOs was that intense measurements of the entire CZ at a few locations would illuminate connections between landscape structure and hydrologic function (Brantley et al., 2017; Jefferson et al., 2014; Kumar et al., 2018; Lohse & Dietrich, 2005; Troch et al., 2015; Yoshida & Troch, 2016). And yet, putting together the disparate measurements at all CZOs has remained elusive at least partly because of the many differences in sites. Here we make a first foray toward understanding and simulating the processes underpinning landscape-hydrological interactions in the hopes that our effort will ultimately foster new approaches for managing water resources (Kumar, 2011; Sivapalan & Blöschl, 2017). Cross-site synthesis is needed to unpack the interactions between landscape structure and hydrologic response, but cross-site comparisons are inherently difficult because of differences in definitions and measurements of important landscape and hydrologic features. Large-sample synthesis studies have sought to build understanding by linking hydrologic signatures to catchment properties (Addor et al., 2017, 2018; Berghuijs et al., 2014, 2016; Sawicz et al., 2011; Sivapalan et al., 2011). We build on this work by focusing on a smaller set of sites with a more detailed documentation of their respective subsurface architectures.

The goals of this paper are to make three key initial steps toward understanding the interactions between critical zone structure and hydrologic function. First, we completed a large effort to compile a common set of hydrologic data for 15 catchments from across the U.S. CZO network for synthesis here and, hopefully, for others in the future. Second, we extracted quantitative signatures of hydrologic function to characterize how they partition, store, and release water. Finally, we examined variability across the sites in the network seeking to highlight patterns. By summarizing cross-network variability in hydrologic behavior, the data sets and analyses presented here contribute to a first small step toward the development of generalizable theories for understanding the partitioning, storage, and transmission of water in the critical zone.

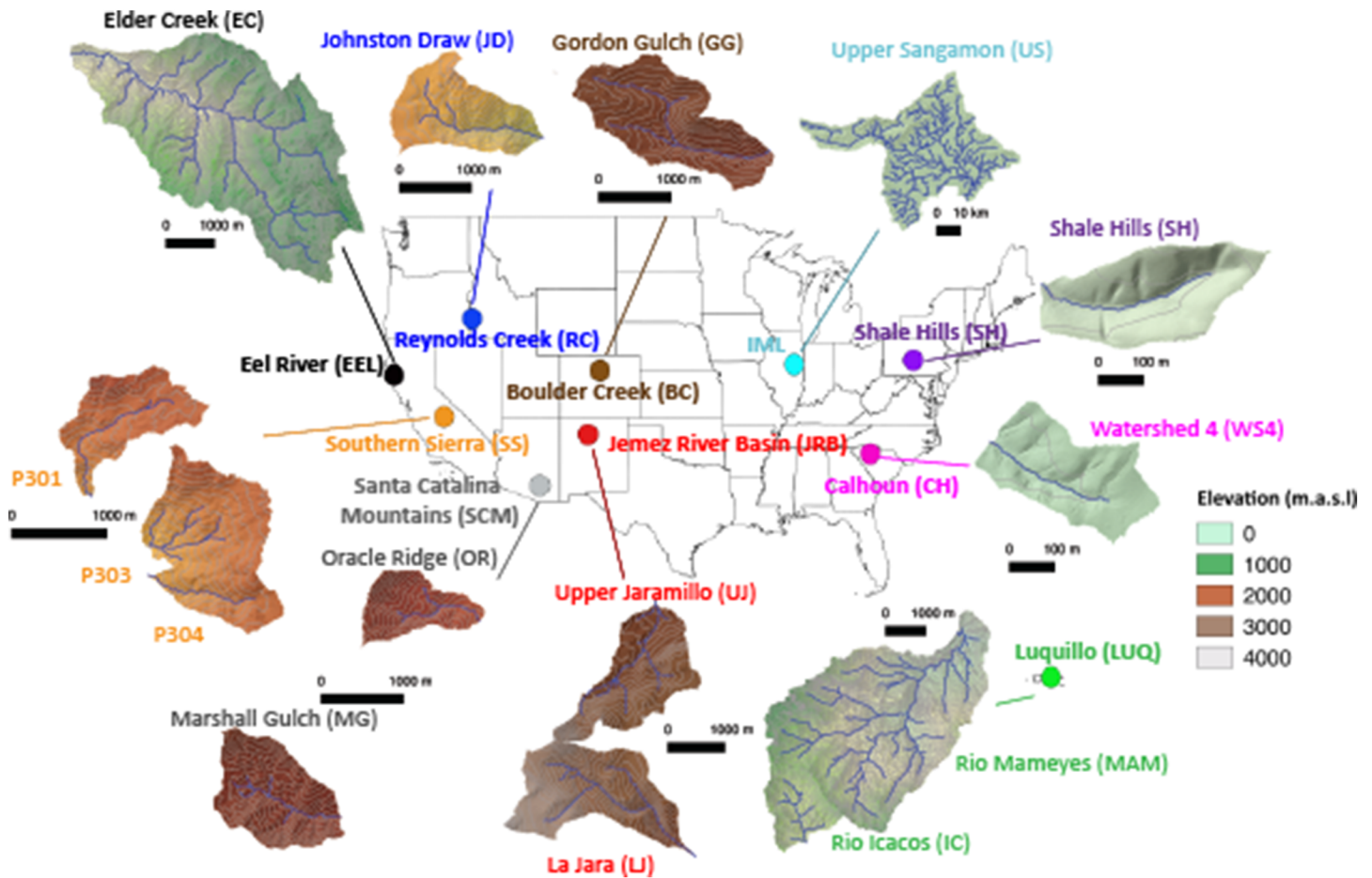


Figure 1. National map of the conterminous United States showing the location of each Critical Zone Observatory (CZO) and subset digital elevation models depicting individual catchments at each CZO considered in this study. Contour lines on catchment maps are at 20-m intervals. Throughout the text, figures, and tables, catchments are referred to by the abbreviations adjacent to CZO and catchment names on this map. For example, Gordon Gulch at the Boulder Creek CZO is referred to as BC (observatory) GG (catchment), and Johnston Draw at Reynolds Creek CZO is referred to as RC (observatory) JD (catchment).

2. The U.S. Critical Zone Observatories

This study considers 15 catchments located across the U.S. CZO network where previous critical zone investigations have been conducted (Figure 1 and Table 1). The collection of catchments is geomorphically, ecologically, and geologically diverse (Table 1). Catchment drainage area varies by over 4 orders of magnitude and median catchment elevation spans nearly 3,000 m. Basin relief ranges from 35 to 966 m and median slope ranges from 1% to 24%. Catchment bedrock composition includes metamorphic, igneous, and sedimentary rock types ranging in age from Precambrian to Quaternary. Land cover, dominant vegetation species, and land use history exhibit similar variation across catchments. For a more detailed review of observatory landscape properties and characteristics, see White et al. (2015).

3. Catchment Storage as Synthesis

Catchment storage dynamics are a logical basis for synthesizing hydrologic function across a set of catchments (McNamara et al., 2011; Staudinger et al., 2017). The filling and spilling of catchment storage space are both a function of contemporary landscape architecture and a characteristic that drives landscape evolution (Beven et al., 1988). However, storage is also largely invisible. The general lack of subsurface characterization available in many catchments hampers our ability to draw meaningful linkages between catchment structure and hydrologic behavior. Catchment water storage can typically only be observed indirectly through hydrologic analysis.

Table 1
Topographic, Vegetation, and Geologic Characteristics of 15 Catchments Across the Critical Zone Observatory Network

Observatory	Catchment name	Area (km ²)	Median elevation (m)	Relief (m)	Median slope (%)	Depth to fresh bedrock (m)	Dominant vegetation	Geologic parent material
Boulder Creek (BC)	Gordon Gulch (GG)	2.77	2,638	270	14	10–14 ^b	Mixed conifer forest, predominantly lodgepole and ponderosa pine	Metamorphic (Precambrian gneiss)
Shale Hills (SH)	Shale Hills (SH)	0.08	283	30	30	16–44 ^a	Oak, hickory, and pine forest	Sedimentary (Silurian shale)
Eel River (ER)	Elder Creek (EC)	16.85	828	867	29	4.5–30 ^c	Douglas-fir, tan oak, and Pacific madrone mixed forest	Sedimentary (Mesozoic argillite)
Jemez River Basin (JRB)	Upper Jaramillo (UJ)	3.05	2,919	601	12	27–34 ^d	Spruce-fir forest and woodland	Extrusive igneous (Quaternary rhyolitic tuff)
Santa Catalina Mountains (SCM)	La Jara (LJ)	3.68	3,086	727	15	42–49 ^d	Mixed conifer and deciduous (oak and maple) forest	Intrusive igneous and metamorphic (Tertiary granite and schist)
	Marshall Gulch (MG)	1.55	2,424	351	24	N/A		
Luquillo (LUQ)	Oracle Ridge (OR)	0.86	2,265	403	21	N/A	Ponderosa pine transitioning to pinyon-juniper-oak forest from high to low elevation	Intrusive igneous (Tertiary quartz monzonite)
	Rio Mameyes (MAM)	17.80	508	967	22	27.7–37.2 ^e	Tabonuco, Palm, and Colorado forest	Sedimentary (Cretaceous volcanics)
Reynolds Creek (RC)	Rio Icacos (IC)	3.26	686	212	14	N/A	Colorado and Palm forest	Intrusive igneous (Tertiary quartz diorite)
	Johnston Draw (JD)	1.83	1,747	374	14	13–31 ^f	Sagebrush grassland with intermittent aspen and juniper stands	Intrusive igneous (Cretaceous granite)
Southern Sierra (SS)	P301	0.99	1,990	318	12	10–35 ^g	Mixed conifer forest	Intrusive igneous (Cretaceous granodiorite)
	P303	1.26	1,906	292	14	N/A		
	P304	0.49	1,909	213	14	N/A		
IML (IML)	Upper Sangamon (US)	615.73	232	88	1	100 ^h	Corn and soybean agricultural rotation	Sedimentary (Silurian to Carboniferous dolomite, shale, limestone, and sandstone beneath thick glacial drift deposits)
Calhoun (CH)	Watershed 4 (WS4)	0.07	163	35	10	8–38 ⁱ	Pine-hardwood forest	Intrusive igneous (Silurian metagranite)

^aDepth of fresh bedrock observed in deep boreholes situated along ridges and valleys of the Shale Hills catchment (Sullivan et al., 2016 and unpublished observations). ^bSeismic refraction surveys along four north-south transects in Gordon Gulch, where the weathered-fresh bedrock boundary was inferred to reside at the 3,500 m/s *P* wave velocity contour (Befus et al., 2011). ^cDepth to fresh bedrock observed in boreholes throughout catchment, deepest depth to fresh bedrock is beneath ridgetops and shallowest depth to bedrock beneath valley bottoms (Hahm et al., 2019; Rempe & Dietrich, 2018; Salve et al., 2012). ^dSeismic refraction surveys along transects in La Jara and Upper Jaramillo catchments, where the regolith to unweathered bedrock transition was inferred to occur at the 2.95 km/s *P* wave velocity contour (Olyphant et al., 2016). ^eDepth to what is inferred to be “relatively unweathered bedrock” in two boreholes (Buss et al., 2013). ^fSeismic refraction surveys along four north-south oriented transects, where the weathered-fresh bedrock boundary is inferred to reside at the 3,500 m/s *P* wave velocity contour (Nielson, 2017). ^gSeismic refraction survey along a single north-south transect, where the weathered-fresh bedrock boundary is inferred to reside at the 4,000 m/s *P* wave velocity contour (Holbrook et al., 2014). ^hBorehole observation (Kumar et al., 2018). ⁱDeep borehole observations at location oriented near ridgetop and seismic refraction survey along a single east-west transect (Holbrook et al., 2019; St. Clair et al., 2015). Depth to bedrock is deepest beneath ridges and shallowest beneath valley bottoms.

Dynamic storage refers to indirectly estimated water storage capacity that is actively filled and drained over timescales relevant to annual input and output fluxes (McNamara et al., 2011). Dynamic storage is inferred by analyzing water fluxes (precipitation, runoff, and evapotranspiration) under a water balance framework. We propose two perspectives on catchment-scale dynamic water storage to serve as a framework for the synthesis study: *terrestrial* and *hydraulic* storage (Carrer et al., 2018; Dralle et al., 2018).

3.1. Terrestrial Storage

Terrestrial storage, s_{terr} [L], is the volume of water stored beneath the land surface as inferred by evaluating a catchment-wide water balance over some timescale. Changes in s_{terr} are controlled by rates of surface water input (SWI [L/T]), runoff (Q [L/T]), evapotranspiration (ET [L/T]), and net groundwater flows (GW [L/T]).

$$\frac{ds_{terr}}{dt} = SWI - Q - ET - GW. \quad (1)$$

SWI is the input of liquid water from aboveground to terrestrial storage. In this conceptual model, we assume that snowpack is an aboveground storage reservoir distinct from s_{terr} . Other aboveground storage reservoirs, such as canopy interception and depression storage, are assumed to be negligible compared to the catchment's total dynamic storage. While this is a major conceptual simplification, it is justified at 11 of 15 CZO catchments due to a substantial influence of snow (e.g., Tennant et al., 2017). In cold regions, the snowpack decouples the timing and intensity of SWI from precipitation (P [L/T]) because accumulated snow is not immediately available for infiltration but is retained until the melt period.

We define SWI as the sum of snow/ice melt, M [L/T], rainfall on snow, P_S [L/T], and direct rainfall, P_D [L/T], which falls directly onto the land surface and is not retained by the snowpack.

$$SWI = M + P_S + P_D \quad (2)$$

At any time, total precipitation, P [L/T], is the sum of surface accumulated precipitation as ice/snow, P_{acc} [L/T], P_S , and P_D .

$$P = P_D + P_{acc} \quad (3)$$

In catchments with no snow/ice accumulation (i.e., $P_{acc} = 0$ and $P_S = 0$), $SWI = P_D = P$.

For convenience, we assume that net groundwater exchange (GW) is a negligible term in Equation 1. This assumption is unlikely to hold for most of the catchments considered in this study—small headwater catchments nested in much larger regional groundwater systems (Fan, 2019; Tóth, 1999). To accurately quantify net groundwater flows in CZO catchments, a more detailed synthesis of hydrogeologic data is needed. In absence of such a synthesis, we move forward with this simplifying assumption and discuss the implications for study results.

Finally, s_{terr} must be defined relative to some initial (and unknown) storage state, s_0 , and is evaluated as a function of time by integrating 1 from some initial time ($t = 0$) to time t .

$$s_{terra} - s_0 = \int_0^t (SWI - Q - ET) dt \quad (4)$$

3.2. Hydraulic Storage

Hydraulic storage, s_h [L], is defined as the storage that drives streamflow generation. Specifically, changes in s_h are hydraulically linked to streamflow through an assumed 1-to-1 relationship. Hydraulic storage is determined from the recession behavior of the streamflow hydrograph using methods developed by Kirchner (2009) and Wittenberg (1999). Dralle et al. (2018) refer to this as “direct storage,” as it is *directly* affiliated with streamflow generation. Hydraulic storage is a subset of s_{terr} because not all stored water is hydraulically linked to flow generation. For example, changes in unsaturated vadose zone storage may have no influence on streamflow generation.

Here we present a formulation of s_h slightly distinct from previous works (e.g., Kirchner, 2009) in the way the role of evapotranspiration is handled. We will assume that the rate of change in s_h with respect to time is controlled by water fluxes into and out of s_h zones:

$$\frac{d s_h}{dt} = R - Q - \alpha ET. \quad (5)$$

Hydraulic storage zones are filled by recharge, R [L/T], and drained by Q and ET . Recharge is conceptually different from SWI , because not all SWI fills hydraulically active storage zones (e.g., the filling of unsaturated zones). Further, not all ET affects hydraulic storage; rather, only a fraction of total catchment ET , α [–], is drawn from hydraulic storage. The influence of evapotranspiration on runoff dynamics is apparent in diel streamflow oscillations and inflated streamflow recession rates as shown by Bart and Hope (2014), Wang and Cai (2010), and Weisman (1977).

Unlike s_{terr} , it is difficult to directly resolve s_h with a water balance approach because R is difficult to observe. Instead, recession curve analysis is used to estimate s_h (Kirchner, 2009; Krier et al., 2012; Teuling et al., 2010). This approach hinges on the assumption that runoff is a single-valued and invertible function of storage.

$$Q = f(s_h) \quad (6)$$

Using the chain rule to differentiate 6 with respect to time and substituting 5 gives an expression for the time rate of change in streamflow:

$$\frac{dQ}{dt} = \frac{dQ}{ds_h} \frac{ds_h}{dt} = g(Q)(R - Q - \alpha ET), \quad (7)$$

where $g(Q) = dQ/ds_h$ [1/T] is the catchment sensitivity function, which quantifies the sensitivity of Q to changes in s_h . Rearranging 7 to solve for $g(Q)$ yields

$$g(Q) = \frac{dQ/dt}{R - Q - \alpha ET}. \quad (8)$$

During periods of extended baseflow recession, it is reasonable to assume that $R \ll Q$ following the redistribution of water from the vadose zone to the water table. During these periods, $g(Q)$ may be directly evaluated from discharge observations using 8 if estimates of αET can be obtained. Once $g(Q)$ is known, the hydraulic storage-discharge relationship, $s_h(Q)$, is estimated by integrating the reciprocal of $g(Q)$ with respect to Q . Similar to s_{terr} , s_h is a dynamic storage term and is defined relative to some initial (and unknown) storage state, s_0 .

$$s_h - s_0 = \int_{Q_0}^Q \frac{1}{g(Q)} dQ \quad (9)$$

4. Data and Methods

4.1. Data Sets Used

A standard set of hydrologic data and estimates (daily precipitation, discharge, potential and actual evapotranspiration, snow water equivalent [SWE], and melt rate) was compiled for the 15 study catchments across the CZO network listed in Table 1. Those data are available for download through the Consortium of Universities for the Advancement of Hydrologic Science, Inc (CUAHSI) HydroShare (Wlostowski et al., 2021). Here we describe how those data were compiled.

Volumetric streamflow data [L^3/T] was obtained from stream gages within each catchment. Detailed information on the location, period of record, drainage area, instrumentation, and data source for each gage is provided in Table S1. Volumetric streamflow is converted to daily runoff [L/T] by normalizing data by catchment area and aggregating subdaily data to a daily time step. At four catchments (LUQ IC, LUQ MAM, EEL EC, and IML US), streamflow is monitored by gages maintained by the U.S Geological Survey (USGS). At these sites, annual runoff is computed by converting USGS estimates of mean annual discharge by normalizing to catchment area. At the remaining sites, annual runoff is calculated by numerical integration of daily runoff data. As such, any gaps in the daily runoff record will lead to underestimates in annual runoff. The variable Q is used to denote daily runoff with units of millimeters per day.

Precipitation data were collated from 27 gages and two spatially distributed precipitation data products (Kormos et al., 2017; Murphy et al., 2017). The location, period of record, and data source for each gage (or data product) are specified in Table S2. By combining available precipitation observations within (or near) each catchment, catchment average daily precipitation intensity is approximated for each site. Table S2 articulates the methodological approach for estimating catchment average daily precipitation intensity at each site. Hereinafter, P is used to denote daily precipitation intensity in units of millimeters per day. The standard deviation of annual precipitation was calculated from the 8-km PRISM product (1895–2019) (PRISM Climate Group, 2019), except at LUQ IC and LUQ MAM, where the available period of record presented in Murphy et al. (2017) was used.

Due to high spatial rainfall variability in the Luquillo Mountains (Murphy et al., 2017) and the lack of long-term daily precipitation gages within the two small Luquillo CZO catchments, a different method of estimating annual and daily precipitation totals was needed. Mean annual precipitation (MAP) was

obtained from Murphy et al. (2017); for LUQ MAM, MAP was estimated by a spatial interpolation of all existing rainfall data, but due to probable underestimation of rainfall in LUQ IC, MAP was estimated from a linear model of annual runoff versus annual precipitation for many tropical forests across the world (Murphy et al., 2017). For LUQ IC and LUQ MAM, daily precipitation at a nearby rain gage (El Verde, <8 km away) was summed to obtain MAP for the period 1995–2015 and scaled to the modeled MAP for each watershed to estimate annual precipitation totals. To approximate daily rainfall intensities for each catchment, daily observations at the El Verde rain gage were scaled by the ratio of annual precipitation in the Rio Mameyes or Rio Icacos to annual precipitation at El Verde. Short-term spatial variability in daily precipitation might cause overprediction/underprediction of daily rainfall intensity in each catchment.

Data from two gridded meteorological products are used in this study. North America Land Data Assimilation System (NLDAS-2) longwave and shortwave radiation, surface pressure, specific humidity, 2-m air temperature, and 10-m wind speed data are used for all catchments located within the continental United States (Mitchell, 2009). NLDAS-2 forcing data have a $1/8^\circ$ spatial resolution and hourly temporal resolution. Data were acquired for all grid cells covering the extent of each catchment. If a catchment extent spans more than one grid cell, the average value of each variable across the total number of grid cells is used. For catchments outside the continental United States (i.e., those in Puerto Rico), Modern-Era Retrospective analysis for Research Applications (MERRA2) data are used. Longwave and shortwave radiation (Global Modeling and Assimilation Office [GMAO], 2015b), air temperature, wind speed, pressure, and specific humidity data (GMAO, 2015a) were obtained at an hourly time step for the single $0.5^\circ \times 0.625^\circ$ grid cell containing both of the Puerto Rico catchments, LUQ IC and LUQ MAM. We opted to use NLDAS-2 and MERRA2 data products in lieu of on-the-ground meteorological observations to enhance methodological consistency and temporal coverage. However, NLDAS-2 and MERRA2 data were bias corrected using available meteorological observations at each site.

Seasonal SWE accumulation/ablation and *SWI* rates are simulated with the SNOW17 model (Anderson, 2006). SNOW17 is a spatially lumped (i.e., assumes uniform spatial distribution of SWE across a catchment) snowpack model that simulates melt rates with a seasonally variable temperature index approach (Hock, 2003). The model is calibrated to match SWE observations at or near each catchment (Table S3). A shuffled-complex evolution algorithm (Duan et al., 1993) is used to exhaustively search the model parameter space and identify near-optimal parameter sets that minimize the root mean squared error between simulated and observed SWE. Where SWE observations are not available (SH SH and IML US), a standard parameterization is used. Model parameter values are presented in Table S3. Once parameter values are established, forward simulations estimate catchment average daily SWE and melt fluxes for each catchment. This spatially lumped approach to SWE modeling is admittedly simplistic, especially at sites where snow cover is spatially and temporally intermittent (e.g., RC and BC). Nevertheless, this approach offers a first-order approximation of basin-average SWE accumulation/ablation dynamics.

MODIS leaf area index (LAI) data (Myneni et al., 2015), which have a 500×500 m spatial resolution and 8-day temporal resolution, were obtained for grid cells covering each catchment. Mean LAI of all grid cells covering a catchment is calculated for every 8-day observation and linearly interpolated to a daily time step. Snow depth and/or SWE data were collated from five CZO sites. Data set names, locations, periods of record, and data sources are provided in Table S4. Digital elevation models are used to characterize the land surface topography of each catchment. Details and data sources of surface topography data sets can be found in Table S4. Soil horizon, depth, and texture data were obtained for each catchment from the Digital General Soil Map of the United States (STATSGO2) (Soil Survey Staff, Natural Resources Conservation Service, U. S. D. of A., 2018).

4.2. Estimating Actual Evapotranspiration

Actual evapotranspiration, ET_a (mm/day), is estimated by scaling surface-dependent potential evapotranspiration, PET_{surf} (mm/day), by the ratio of the average deficit between annual precipitation, P_{ann} (mm), and annual runoff, Q_{ann} (mm), to average annual PET_{surf} .

$$ET_a = PET_{surf} \frac{\overline{P_{ann} - Q_{ann}}}{\overline{PET_{surf, ann}}}, \quad (10)$$

where $PET_{surf,ann}$ is total annual surface-dependent potential evapotranspiration (mm). PET_{surf} is calculated using a surface-dependent Penman-Monteith model (Monteith, 1973), forced with daily average meteorological data (section 5.1). Aerodynamic and canopy resistance terms in the model are dependent on land surface characteristics. Specifically, aerodynamic resistance is a function of vegetation height (Monteith, 1965), and canopy resistance is assumed to be a function of LAI (Shuttleworth & Wallace, 1985). Following Shuttleworth and Wallace (1985), mean stomatal conductance was set to 400 s/m at all sites for simplicity. Differences in vegetation between sites likely render a spatially constant value of stomatal conductance inappropriate, though we proceed for convenience's sake.

This approach for estimating ET_a assumes that actual evapotranspiration is approximately equal to the long-term mean deficit between P and Q (Budyko, 1974). Furthermore, this approach assumes that the seasonality of ET_a is identical to the seasonality of PET_{surf} . These assumptions are least plausible for catchments with substantial groundwater gains/losses, short periods of record focused on anomalously wet or dry periods, and/or catchments with significant intra-annual variations in water/energy limitation.

4.3. Hydroclimatic Indices

The aridity index (AI) is calculated as the ratio of annual reference land cover potential evapotranspiration, $PET_{ref, ann}$ (mm), to P_{ann} (Budyko, 1974).

$$AI = \frac{PET_{ref, ann}}{P_{ann}} \quad (11)$$

PET_{ref} (mm/day) is calculated from a Penman model with a “reference crop” run at a daily time step (Penman, 1947), forced by daily average meteorological data. Unlike PET_{surf} , between-site variations in PET_{ref} are only due to climatic differences because PET_{ref} assumes that land cover is homogeneous across sites (reference crop), making AI a purely climatic metric.

The seasonality index, ϕ , summarizes the relative timing and magnitude of terrestrial water supply (SWI) and evaporative demand (PET) (Woods, 2009):

$$\phi = A_{SWI} \text{sgn}(A_{PET_{ref}}) \cos(2\pi(\theta_{SWI} - \theta_{PET_{ref}})/365), \quad (12)$$

where A_{SWI} and θ_{SWI} are the amplitude and time offset of mean annual SWI variation and $A_{PET_{ref}}$ and $\theta_{PET_{ref}}$ are the amplitude and time offset of mean annual PET_{ref} variation. A_{SWI} , θ_{SWI} , $A_{PET_{ref}}$, and $\theta_{PET_{ref}}$ are determined by fitting sinusoidal models through time series of mean SWI and PET_{ref} for each day of the water year (1 October through 30 September). Sinusoidal models of annual SWI and PET_{ref} variation are denoted as SWI' and PET'_{ref} , respectively:

$$SWI'(t) = \overline{SWI} [1 + A_{SWI} \sin(2\pi(t - \theta_{SWI})/365)] \quad (13)$$

$$PET'_{ref}(t) = \overline{PET_{ref}} [1 + A_{PET_{ref}} \sin(2\pi(t - \theta_{PET_{ref}})/365)]. \quad (14)$$

The seasonality index, ϕ , is strongly sensitive to the phase lag between water supply (SWI) and demand (PET_{ref}). When supply and demand are out of phase, ϕ is negative. Conversely, when supply and demand are in-phase, ϕ is positive. Additionally, the magnitude of ϕ is sensitive to A_{SWI} . Catchments with no seasonal SWI variation (i.e., same SWI intensity every day of the year) have A_{SWI} and ϕ equal to zero.

Automated baseflow separation is used to partition hydrographs into baseflow and storm flow. The baseflow index (BFI) is the ratio of baseflow to total streamflow over the available period of record. We partition baseflow from observed hydrographs using a single-pass digital filter technique (Arnold & Allen, 1999).

4.4. Hydraulic Storage Calculation

Hydraulic storage is calculated from the catchment sensitivity function, $g(Q)$, which is derived from streamflow recession observations using 8. Other analyses of this type (Kirchner, 2009) use recession observations

when $ET_a \ll Q$, and therefore, $ds_h/dt \approx -Q$. Further, $g(Q)$ is estimated as a continuous function of Q by fitting an empirical model through recession plot observations ($-dQ/dt$ v. Q) and dividing the model by Q . However, in arid and semi-arid catchments, ET_a is rarely much less than Q leaving little (or no) observations remaining from which to derive $g(Q)$. In 10 of the 15 catchments considered in this work, ET_a is much greater than Q for over 90% of all Q observations. At these catchments, it is critically necessary to account for the influence of ET on $g(Q)$.

To account for the influence of ET on $g(Q)$, we compute an ET -adjusted recession rate, ε (mm/day²):

$$\varepsilon = \frac{-dQ/dt}{Q + \alpha ET} Q, \quad (15)$$

where α is the fraction ET_a drawn from s_h . If αET_a is negligible relative to Q , ε reduces to $-dQ/dt$. Physically, we might expect this to be the case when water table levels are lower than the rooting depth of catchment vegetation. However, if αET_a is comparable in magnitude to Q , then the ε is less than $-dQ/dt$. We might expect this to be the case when water table levels intersect the rooting zone, and plant water use is drawn from the same storage compartments involved in runoff generation. In this work, we arbitrarily set $\alpha = 0.25$ and test the sensitivity of s_h to α by setting α to end-member values, 0 and 1.

We define recession periods as times when $SWT = 0$, simulated $SWE = 0$, and the recession duration is at least 4 days (Figure 2a). For all daily recession period observations, $-dQ/dt$ is estimated with a 3-day sliding window regression and ε is calculated using 15. Daily ε values are plotted against daily Q observations to create ET -adjusted recession plots (Figure 2b). Following Kirchner (2009), daily ε values are grouped into 100 logarithmically distributed Q bins. Bins are merged with adjacent bins until each bin has at least three ε estimates and the standard error of ε in any bin is less than half of the mean of ε in that bin. Binned ε values (ε_{bin}) are plotted as red markers in Figure 2b.

A novel dynamic power law function, ε_{fit} , is fit through the binned ε estimates to empirically describe the variation of ε as function of Q (Figure 2b; Equations 16 and 17).

$$\varepsilon_{fit} = a \left(\frac{Q}{\bar{Q}} \right)^{b(Q)}, \quad (16)$$

where

$$b(Q) = b_L + (b_U + b_L) \frac{1}{2} \left[1 + \operatorname{erf} \left(\frac{\ln(Q) - \ln(\bar{Q})}{\ln(\sigma) \sqrt{2}} \right) \right]. \quad (17)$$

The power law exponent, b , in 17 is a sigmoidal function of Q (Equation 17), ranging from b_U and b_L following a lognormal cumulative distribution of Q with mean and standard deviation $\ln(\sigma)$ (Figure 3a). When $b_L = b_U$, $\ln(\varepsilon_{fit})$ v. $\ln(Q)$ plots as a straight line. When $b_U > b_L$, the slope of $\ln(\varepsilon_{fit})$ v. $\ln(Q)$ is variable, steeper at high flows, and more gradual at low flows (Figure 3b). The variability of b makes 16 and 17 sufficiently flexible to fit nonlinear trends observed commonly in log-log recession plots.

The catchment sensitivity function is finally derived as

$$g(Q) = \frac{\varepsilon_{fit}}{Q}. \quad (18)$$

The relationship between hydraulic storage and Q is derived by integrating the reciprocal of $g(Q)$ from the minimum nonzero Q (Q_{min}) to the 99th percentile flow rate (Q_{99}) and appointing an arbitrary initial storage state (s_0) (Figure 2c).

$$s_h(Q) = \int_{Q_{min}}^{Q_{99}} \frac{1}{g(Q)} dQ + s_0(Q_{min}). \quad (19)$$

The absolute value of s_0 and s_h cannot be known, but s_0 was selected such that the median of s_h was zero. The 99th percentile flow rate is used as the upper integration boundary instead of the peak flow, because

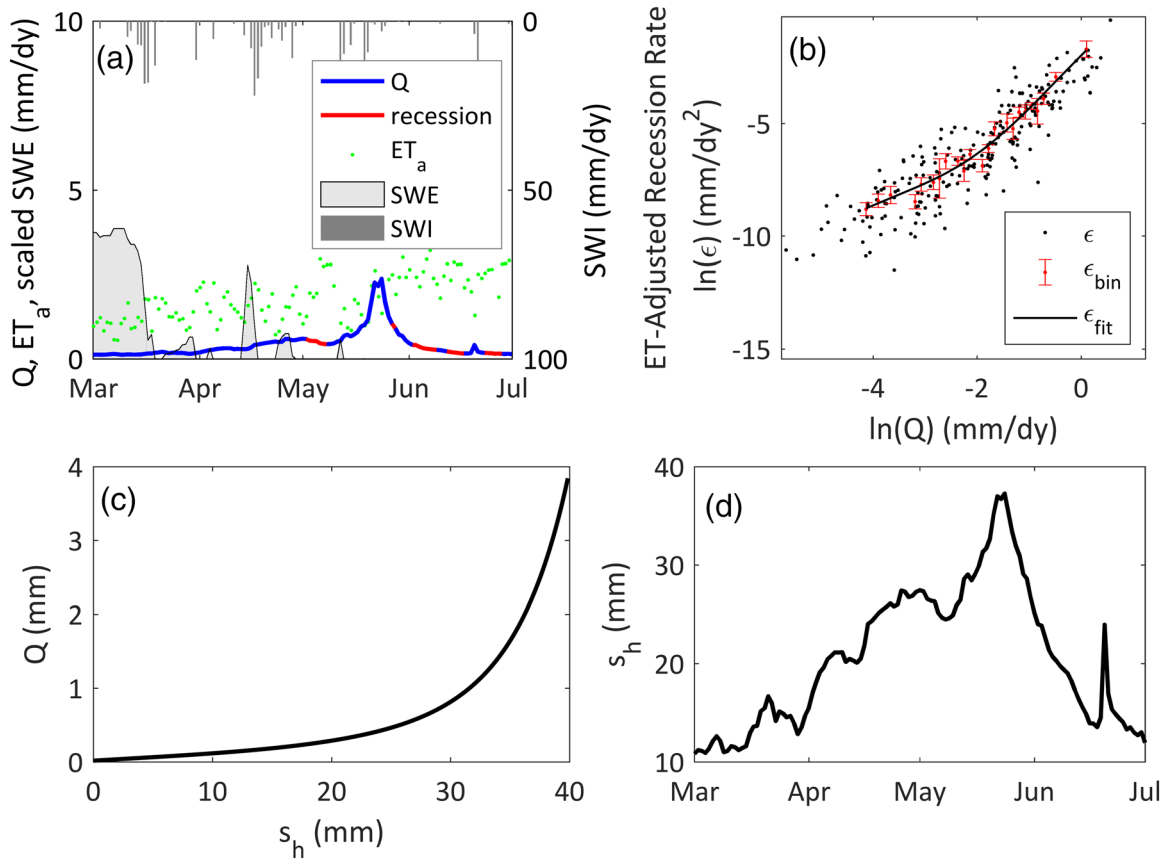


Figure 2. (a) Streamflow recession periods are extracted from the hydrograph by finding times when there is no snow on the ground, $SWI = 0$, and streamflow continuously recedes for at least 3 days. (b) A dynamic power law function describes the relationship between $\ln(\epsilon)$ and $\ln(Q)$ by fitting $\ln(\epsilon_{bin})$ and $\ln(Q_{bin})$. (c) The hydraulic storage-discharge relationship is calculated by integrating the reciprocal of $g(Q)$ from $Q_{min} > 0$ to Q_{99} , informed and uninformed parts of the relationship are shown. (d) Hydraulic storage-discharge relationships are used to transform $Q(t)$ to $s_h(t)$. Hydraulic storage estimates are not made for $Q > Q_{99}$. The data shown in this figure are from a single water year at Boulder Creek's Gordon Gulch catchment.

extremely high flows are usually associated quick-flow processes that bypass storage zones (e.g., overland flow). Equation 19 is used to map $Q(t)$ to $s_h(t)$ (Figure 2d). It is important to note that $s_h(Q)$ is only informed by recession Q data, a small subset of all the Q data indicated by a red line in Figure 2c. Estimating s_h beyond the range of recession Q requires extrapolation of ϵ_{fit} .

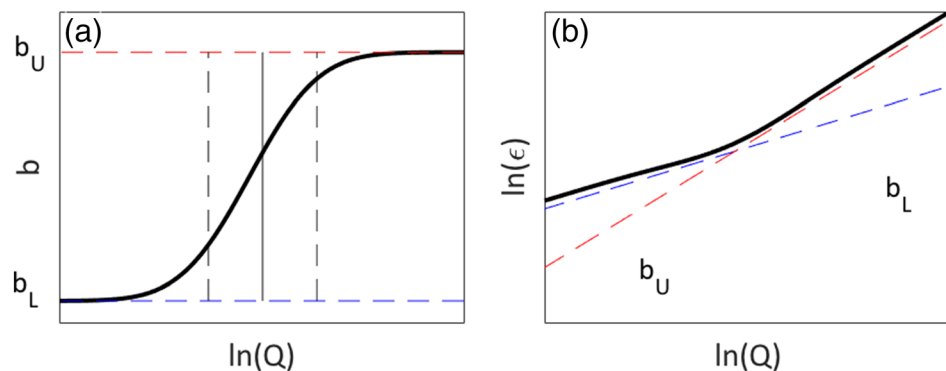


Figure 3. (a) Power law exponent, b , is a lognormal cumulative distribution function of $\ln(Q)$. In the example shown, $b_L < b_U$ resulting in an increasing cumulative distribution from low to high Q . (b) Changes in b as a function of $\ln(Q)$ lead to nonlinear $\ln(\epsilon)$ v. $\ln(Q)$ shapes. Dashed lines show $\ln(\epsilon)$ v. $\ln(Q)$ shapes resulting if $b = b_U$ and $b = b_L$.

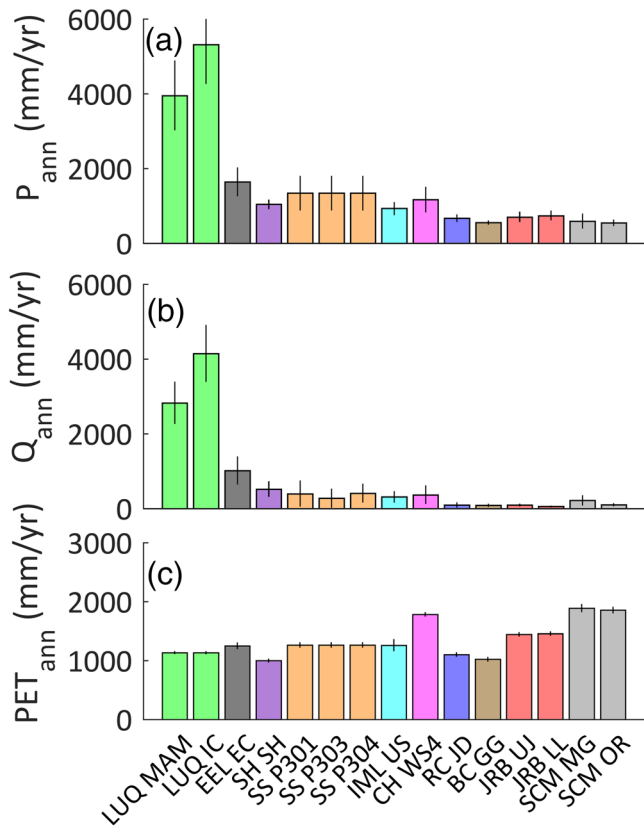


Figure 4. Mean annual precipitation (a), runoff (b), and reference-surface potential evapotranspiration (c) for 15 catchments across the CZO network. Error bars indicated ± 1 standard deviation above and below mean values and sites are arranged from left to right by order of increasing aridity.

5. Results

5.1. Annual Water Partitioning and Hydroclimatic Seasonality

MAP ($\overline{P_{ann}}$), runoff ($\overline{Q_{ann}}$), reference-surface potential evapotranspiration ($\overline{PET_{ref,ann}}$), and actual evapotranspiration ($\overline{ET_{a,ann}}$) vary strongly among network catchments (Figure 4 and Table 2). MAP (Table 2 and Figure 4a) varies by an order of magnitude from 546 mm/yr at SCM OR (see Table 1 for catchment abbreviations) to 5,313 mm/yr at LUQ IC. Mean annual runoff (Table 2 and Figure 4b) varies from 56 mm/yr at JRB LJ to 4,151 mm/yr at LUQ IC. Mean annual reference-surface potential evapotranspiration (Table 2 and Figure 4c) ranges from 1,002 mm/yr at SH SH to 1,889 mm/yr at SC MG and 1,854 mm/yr at SC OR. Mean annual actual evapotranspiration, as approximated by an interannual water balance (Table 2), spans from 376 mm/yr at SCM MG to 1,162 mm/yr at LUQ IC.

It is important to note that annual ET_a estimates are solely based on the long-term difference between P and Q (Equation 10, Table 2) and will therefore be biased by groundwater gains/losses or multiyear changes in net storage. The consequence of this assumption becomes apparent by comparing annual ET_a estimates from this work to independently derived estimates of actual evapotranspiration synthesized from the literature (Table 2, $ET_{a,ann}$ literature). For example, flux tower derived annual ET_a at SS range from 500 to 800 mm/yr (Bales et al., 2018), which are much greater than ET_a estimated by 10. Such a discrepancy may be caused by shallow or deep groundwater losses, which are not explicitly accounted for in the water balance approach used in this study.

The aridity index (AI) is a first-order control on long-term mean annual water partitioning, as illustrated by Figure 5. Network catchments occupy a wide range of AI , from 0.22 (LUQ IC) to 3.63 (SCM MG). Generally, as AI increases, a smaller fraction of P_{ann} is partitioned to Q_{ann} . Accordingly, the long-term mean annual water balance (larger markers in Figure 5b)

coarsely follows Budyko's function ($\pm 20\%$; Li et al., 2014), an empirical function describing a nearly ubiquitous relationship between mean annual water balance and AI (Budyko, 1974). However, three catchments (SH SH, EEL EC, and SCM MG) deviate from Budyko's function, plotting below the 20% error boundary. Deviations below the Budyko function indicate an "overproduction" of runoff relative to Budyko's hypothesis.

Temporal patterns of annual SWI and PET_{surf} are diverse among network sites (Figure 6). Four CZOs (EEL, RC, SS, and CH) exhibit Mediterranean-type hydroclimatic regimes, where SWI is highest during the winter while PET_{surf} is lowest. At BC, JRB, and SCM, summer monsoon storms act to coalign the timing of SWI and PET_{surf} . At these sites, annual precipitation is bimodal and poorly fit by a sinusoidal model (Figure 6). Similarly, at IML and SH, the lag time between SWI and PET_{surf} is reduced by spring and summer rains. In contrast to other network sites, there is relatively little variation of SWI and PET_{ref} at LUQ, yet SWI and PET_{surf} are approximately in phase. Seasonal water delivery and demand dynamics are summarized by the seasonality index (ϕ , Equation 12), which ranges from -1.06 at EEL (strongly out of phase) to 0.46 at SCM (moderately in phase) (Table 2).

5.2. Terrestrial Storage Distributions

Terrestrial storage (s_{terr}) is evaluated at a daily time step for each catchment using 4. Boxplots of median-adjusted s_{terr} distributions are plotted in Figure 7 as a way of comparing s_{terr} states among catchments. The range of s_{terr} distributions (vertical lines in Figure 7) conveys the total dynamic s_{terr} capacity of each catchment. In Figure 7, boxplot ranges include negative values because s_{terr} is a relative, not absolute, term. The interquartile range (IQR) of each distribution, indicated by the vertical extent of the boxes in

Table 2
Mean Annual Water Fluxes and Seasonality Indices for 15 Critical Zone Observatory Catchments

Catchment	Record years	$\overline{P_{ann}}$ (mm)	$s(P_{ann})$ (mm) ^b	$\overline{Q_{ann}}$ (mm)	$\overline{PET_{ref,ann}}$ (mm)	$\overline{ET_{a,ann}}$ (mm)	$\overline{ET_{a,ann}}$ literature (mm) ^c	Aridity index	Seasonality index, ϕ	Annual snow fraction ^k (%), mean (std)
LUQ IC	1995 – 2014	5,313	1,021	4,151	1,135	1,162	306 – 1904 ^d	0.22	0.17	0
LUQ MAM	1995 – 2014	3,953	760	2,883	1,135	1,052		0.30		
EEL EC	2009 – 2016 ^a	1,636	556	1,012	1,254	624	339 – 514 ^e	0.81	–1.06	0
SH SH	2006 – 2012	1,036	144	520	1,002	516	391 – 566 ^f	0.98	0.24	25 (5)
SS P301	2004 – 2010	1,336	310	399	1,267	937	500 – 800 ^g	1.06	–1.04	72 (14)
SS P303	2004 – 2010	1,336	310	276	1,267	1,060		1.06		
SS P304	2004 – 2010	1,336	310	410	1,267	926		1.06		
IML US	2000 – 2015	926	147	317	1,263	609	416 – 618 ^h	1.40	0.36	16 (4)
CH WS4	2015 – 2016	1,164	197	369	1,782	795	N/A	1.61	–0.22	0
RC JD	2003 – 2015	674	139	96	1,105	578	150 – 491 ⁱ	1.67	–0.47	62 (9)
BC GG	2010 – 2013	557	93	86	1,023	470	N/A	1.85	0.41	47 (8)
JRB UJ	2008 – 2015	704	143	97	1,447	607	433 – 465 ^j	2.13	0.45	40 (12)
JRB LJ	2008 – 2012	742	125	56	1,461	686		2.02		
SCM OR	2012 – 2015	546	235	103	1,854	443	N/A	3.46	0.46	29 (5)
SCM MG	2008 – 2015	594	239	218	1,889	376		3.49		

Note. Mean annual runoff, $\overline{Q_{ann}}$, precipitation $\overline{P_{ann}}$, and potential evapotranspiration, $\overline{PET_{ann}}$, are calculated over consecutive record years when all three observations are available.

^aLower than average annual precipitation across California was recorded from 2012 to 2015. As a result, the average annual precipitation and streamflow totals reported for the period of record at EEL EC are lower than the longer-term average reported by Hahm et al. (2019). ^bStandard deviation of annual precipitation calculated from PRISM 1895 – 2019 product (PRISM Climate Group, 2019) at all sites except for LUQ IC and LUQ MAM, which are outside of the PRISM domain. Standard deviation of annual precipitation at LUQ IC and LUQ MAM was calculated from the available precipitation record synthesized by Murphy et al. (2017). ^cAnnual actual evapotranspiration estimates from various literature sources. ^dSynthesized by Murphy and Stallard (2012) and Murphy et al. (2017). ^eWater balance-derived estimates from Salve et al. (2012). ^fModel-derived estimate from Shi et al. (2013) and flux tower-derived estimates using Davis and Shi (2019). ^gFlux tower-derived estimates from Bales et al. (2018). ^hFlux tower-derived estimates using Meyers (2019). ⁱModel-derived estimates from Stephenson and Freeze (1974) and flux tower-derived estimates using Flerchinger (2019). ^jFlux tower-derived estimates using Litvak (2019). Flux tower record includes a pre- and post-fire period. ^kAnnual snow fraction is the percentage of total annual precipitation falling as snow. This is calculated based on a temperature threshold approach in the SNOW17 model and may differ from other independent estimates of snow fraction.

Figure 7, is used as a metric of dynamic s_{terr} capacity. Terrestrial storage IQR ranges from 93 mm at SCM to 560 mm at SS P301.

5.3. Recession Plots and Hydraulic Storage-Discharge Relationships

Recession plots, the log of ET -adjusted recession rates (Equation 15) plotted as a function of $\ln(Q)$, are unique signatures of drainage from hydraulic storage (Figure 8). Recession data shown in Figure 8 assume $\alpha = 0.25$ at all times for all catchments. A dynamic power law model (Equations 16 and 17) quantifies the general shape of recession plots (Figure 3, black lines). The average of b_U and b_L model parameters (b_{av} , Table 3) describes the steepness of recession plots. Higher b_{av} values correspond to more steeply sloping recession plots than lower b_{av} values. The most steeply sloping recession plots are observed in four catchments (LUQ MAM, LUQ IC, SCM OR, and JRB UJ) that have b_{av} values greater than 2 (Table 3). The nonlinearity of a recession plot in logarithmic space is summarized by the difference between b_U and b_L (b_{curve} , Table 3). Five catchments (SS P301, SS P303, SS P304, EEL EC, and IML US) have nearly log-linear recession plot shapes, as indicated by b_{curve} values below 0.2. Another five catchments (JRB LJ, JRB UJ, SCM OR, LUQ IC, and LUQ MAM) have recession plots that are concave downward, as indicated by negative b_{curve} values. All other catchments exhibit concave upward recession plot shapes (Figure 8).

The coefficient of determination (R^2) is used to assess the goodness of fit between dynamic power law models and observed recession data. Coefficients of determination are calculated for comparing models against binned recession observations ($R^2 \epsilon_{bin}$, Table 3) and comparing models against discrete recession observations ($R^2 \epsilon$, Table 3). Models produce satisfactory fits to ϵ_{bin} at all catchments as indicated by $R^2 \epsilon_{bin}$ greater than or equal to 0.6. However, the ability for models to fit clouds of discrete ET -adjusted recession

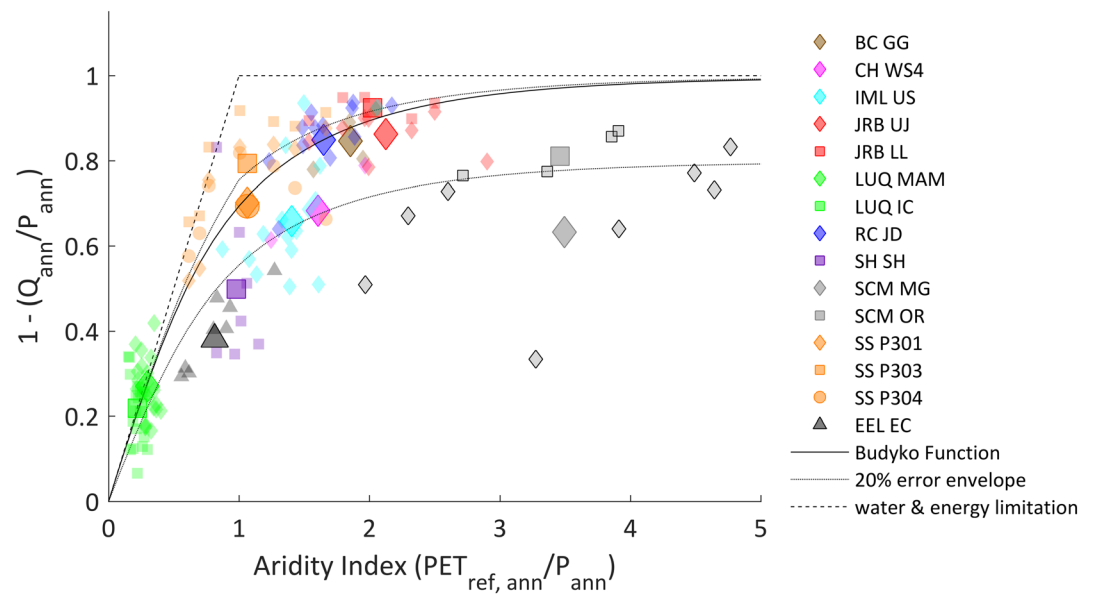


Figure 5. Catchment evaporative partitioning (approximated as $1 - Q_{ann}/P_{ann}$) as a function of the aridity index, also known as a Budyko plot. Smaller markers indicate individual water years, and larger markers denote long-term interannual mean values. Most of the interannual data fall within the theoretical bounds of water and energy limitation, indicated by diagonal and horizontal dashed lines, respectively. Budyko's curve is plotted as a solid black line, with gray lines denoting 20% uncertainty bounds about the feasible range. Ten of 15 catchments fall within the 20% uncertainty bounds of Budyko's curve.

observations is variable between catchments. Models explain less than 50% of the $\ln(\epsilon)$ variance at three catchments (JRB LJ, SCM OR, and LUQ IC). At one of these (JRB LJ), $R^2 \epsilon$ is less than 0, indicating that the model is no better than the mean. Conversely, models produce satisfactory fits to $\ln(\epsilon)$ at five catchments (BC GG, SS P301, SS P303, RC JD, and IML US), where $R^2 \epsilon$ is greater than 0.8. The discrepancy of $R^2 \epsilon$ between catchments calls into question whether recession analysis is appropriate for all catchments.

Hydraulic storage-discharge relationships shown in Figure 9 highlight differing hydraulic storage dynamics among catchments. The total dynamic range of s_h is highly variable between catchments. For example, while RC JD and BC GG span similar ranges of discharge, the dynamic range of s_h is much narrower at BC GG, implying that runoff is more sensitive to changes in s_h . The narrowest dynamic ranges of s_h are observed at SH SH and CH WS4, where runoff is extremely responsive to s_h . Except for JRB LJ, all s_h - Q relationships exhibit increasing concave upward shapes. While the shape of s_h - Q at JRB LJ is unique, the validity of the relationship is questionable because the dynamic power law model poorly fits recession plot data at this site (Table 3). The nonlinear increasing concave upward shape of s_h - Q relationships implies that discharge becomes more sensitive to changes in s_h as s_h increases.

5.4. Hydraulic Storage and Catchment Sensitivity Distributions

Hydraulic storage-discharge relationships (Figure 9) display the total range of s_h states occupied by each catchment. As storage is filled and drained, catchments dynamically navigate the s_h state space. Distributions of s_h encountered by each catchment are summarized with boxplots in Figure 10. The widest IQR of s_h is observed at four catchments (EEL EC, SS P301, P303, and P304), which also exhibit the widest ranges of s_{terr} (Figure 7). These catchments exhibit the widest dynamic storage ranges. The narrowest IQR of s_h is observed at two catchments (CH WS4 and SH SH). As expected, the range of s_h variation at any catchment is less than the range of s_{terr} variation (Figure 7).

Catchment sensitivity $g(Q)$ (day^{-1}) (Equation 18) describes the sensitivity of runoff to changes in hydraulic storage (i.e., the derivative of s_h - Q curves). Curvilinear s_h - Q shapes indicate that catchment sensitivity depends on hydraulic storage state (or Q). Using 18, $g(Q)$ is evaluated for all Q observations at each site.

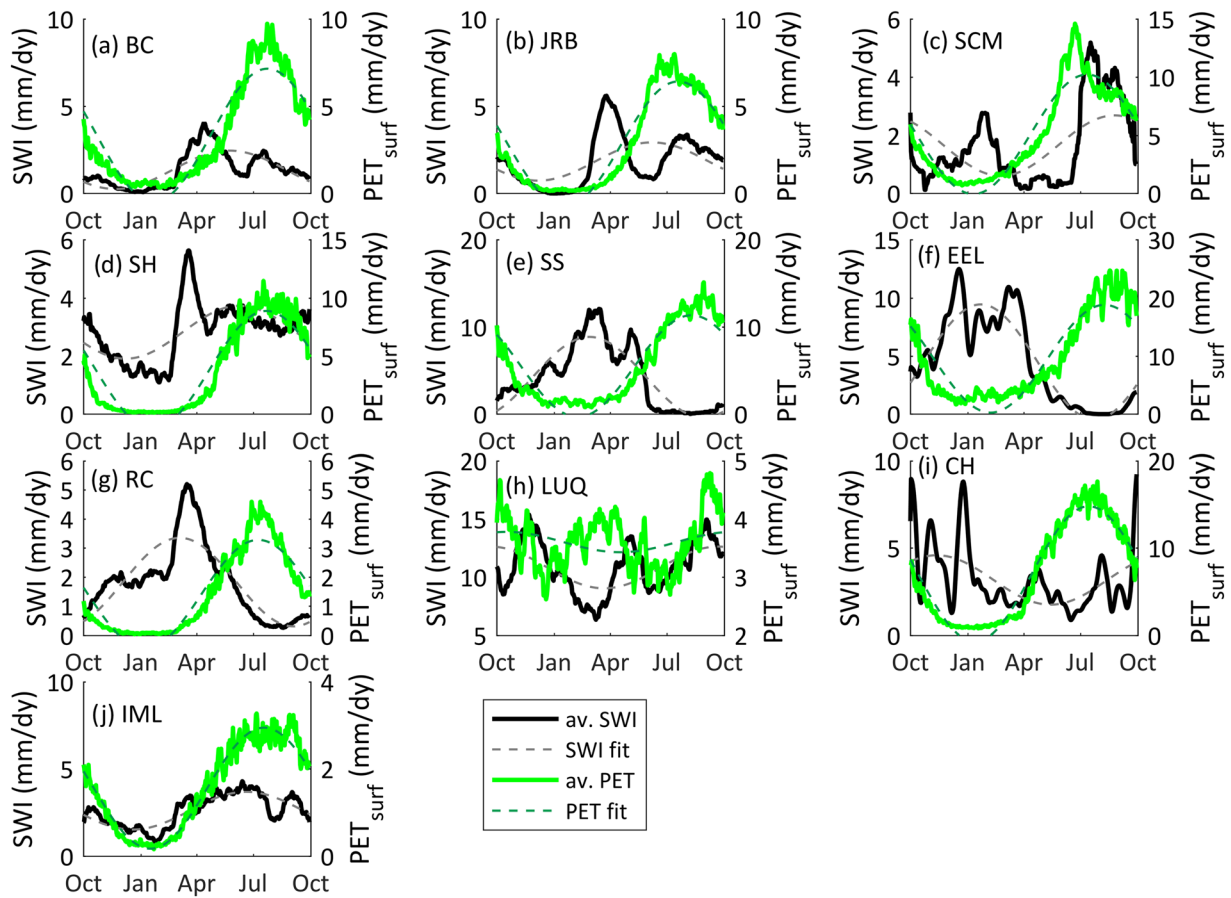


Figure 6. Thirty-day moving window average annual terrestrial water input (SWI , solid black lines) and surface-dependent potential evapotranspiration (PET_{surf} , solid green lines) with best-fitting sinusoidal models (dashed lines) for each observatory.

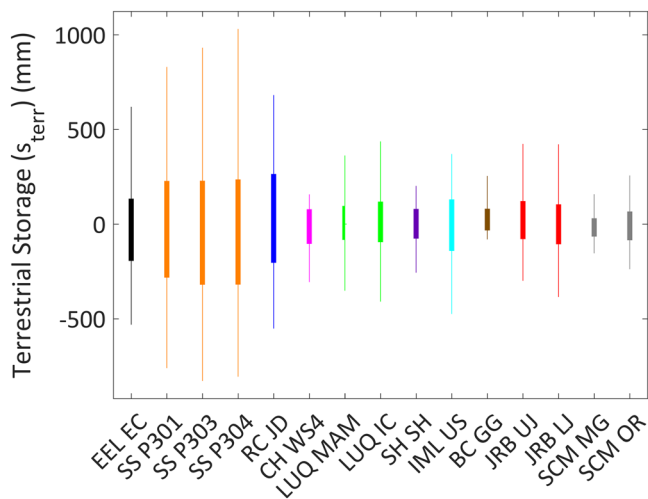


Figure 7. Median-adjusted boxplots summarizing terrestrial storage distributions at 15 CZO catchments. Boxes span the interquartile range and vertical lines show the distribution extent. Sites are arranged from left to right along the x axis in order of increasing seasonality index magnitude. Mediterranean sites are on the leftside of the x axis, whereas monsoonal sites are on the rightside of the x axis.

Sensitivity distributions are summarized by boxplots in Figure 11. Median catchment sensitivity is highest at LUQ, SH, and CH. Conversely, median catchment sensitivity is lowest at JRB LJ, RC JD, SS P303, and SS P304. RC JD, EEL EC, and IML US exhibit the widest IQRs of catchment sensitivity.

The logarithm of median catchment sensitivity is negatively related to baseflow index (BFI) (Figure 12, $p < 0.01$, $R^2 = 0.55$). The highest BFI is observed at SS and JRB catchments and these catchments also exhibit low median $g(Q)$. Conversely, the lowest BFI is observed at SH SH and CH WS4, which also exhibit high median $g(Q)$.

5.5. Relationship Between Dynamic Storage Range and Hydroclimatic Seasonality

The functional ranges of s_{terr} and s_h are widely variable among catchments (Figures 7 and 10). The IQRs of s_{terr} and s_h distributions are significantly correlated with ϕ (Figure 13). Where ϕ is lower (more negative, meaning that surface water inputs and vegetation water demand are seasonally out of phase), wider ranges of s_{terr} and s_h are observed. Where ϕ is greater (more positive, meaning surface water inputs and vegetation water demand are seasonally in phase), narrower ranges of s_{terr} and s_h are observed. This result is somewhat intuitive. Under Mediterranean-type climates, storage is continuously filled during wet winters and then

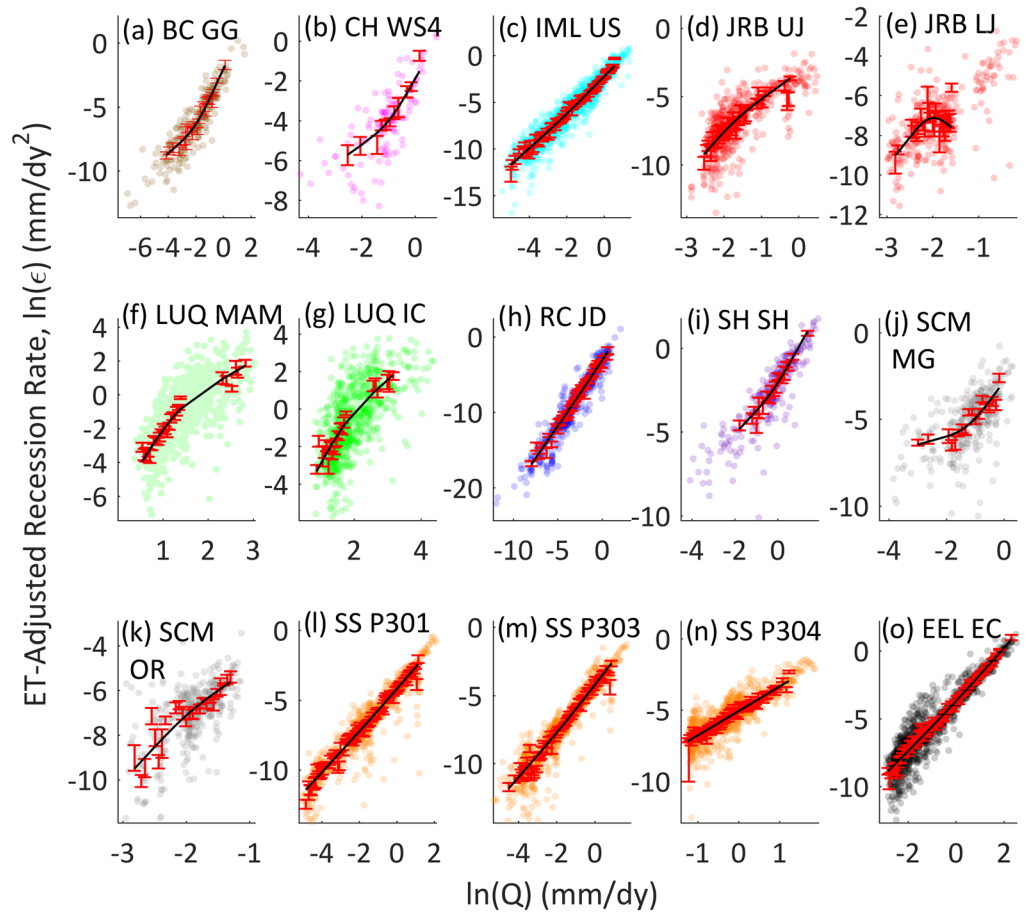


Figure 8. ET-adjusted recession observations (ϵ in Equation 15, colored dots) and binned recession values (red markers) plotted as a function of $\ln(Q)$. Best-fitting regression models are shown as black lines. Axis extents are different on each subplot to accentuate differences in recession plot shape.

Table 3
Dynamic Power Law Regression Model Best-Fit Parameters, Shape Metrics, and Goodness of Fit Statistics

Catchment ID	b_U	b_L	a	b_{curve}	b_{av}	$R^2 \epsilon_{bin}$	$R^2 \epsilon$
RC JD	1.77	1.71	4,633.60	0.06	1.74	0.99	0.90
SS P301	1.54	1.47	837.89	0.07	1.51	0.99	0.86
SS P303	1.80	1.64	1,253.28	0.16	1.72	0.99	0.86
IML US	2.00	1.82	552.06	0.18	1.91	0.99	0.86
BC GG	2.22	1.10	580.98	1.12	1.66	0.98	0.80
SH SH	2.19	1.47	12.62	0.71	1.83	0.98	0.78
EEL EC	1.95	1.80	108.16	0.15	1.88	1.00	0.78
CH WS4	2.22	1.08	55.17	1.13	1.65	0.99	0.62
JRB UJ	2.07	2.99	757.84	-0.93	2.53	0.96	0.59
SCM MG	2.12	0.63	208.72	1.48	1.37	0.86	0.57
SS P304	1.73	1.70	208.29	0.02	1.71	0.97	0.56
LUQ MAM	1.80	4.03	2.87	-2.23	2.92	0.98	0.53
LUQ IC	1.77	3.09	2.02	-1.32	2.43	0.96	0.41
SCM OR	2.09	2.94	1,216.58	-0.85	2.52	0.89	0.33
JRB LJ	-1.39	2.46	1,257.99	-3.85	0.54	0.64	-0.30

Note. Table rows are organized from best to worst R^2 statistic for the model fit against discrete observations.

drained by evapotranspiration throughout dry summers when vegetation water use is highest, causing wide variations in dynamic storage (e.g., EEL EC; Dralle et al., 2018; Hahm et al., 2019). Conversely, the filling and draining of storage zones occurs coincidentally under humid and monsoonal hydroclimatic regimes, when surface water inputs are coincident with periods of high vegetative water use, leading to relatively small ranges of dynamic storage.

The contrasting ranges of s_{terr} and s_h is emphasized by Figure 13c. The IQR of s_h varies between 132 and 9 mm. The IQR of s_{terr} varies between 560 and 93 mm. At all catchments, IQR (s_h) is less than IQR (s_{terr}). The ratio of IQR (s_h) to IQR (s_{terr}) is greatest at EEL EC (0.30) and smallest at CH WS4 (0.05). The hydraulically active storage range accounts for a minority of the total dynamic storage range at each catchment, suggesting that vegetation water use is a sizeable draw on catchment storage reserves.

6. Discussion

The striking spatial variations this analysis has revealed show that the CZOs represent a wide range of hydroclimatic variability. Here we will discuss potential linkages between this variety in functional hydrologic

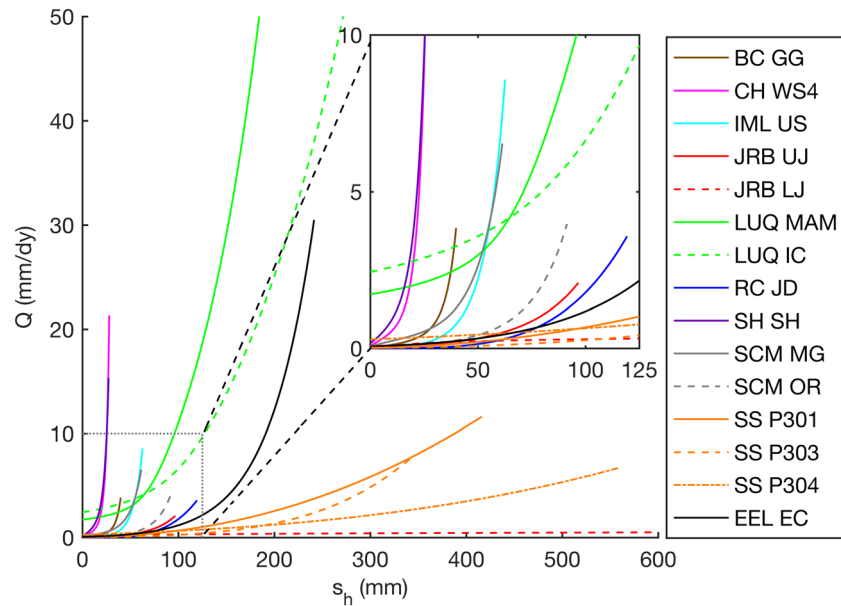


Figure 9. Hydraulic storage (s_h)-discharge (Q) relationships for 15 CZO catchments. The inset plot zooms into lower ranges of s_h and Q in order to highlight the nature of s_h - Q shapes at low-storage catchments.

behavior and variations in critical zone architecture across the sites. Continuing the theme developed throughout the paper, this discussion focuses on dimensions of hydrologic storage as a key functional property of the critical zone.

We can examine the results through two lenses. The first is to consider the annual water balance in terms of the Budyko curve. This well-studied empirical relationship is believed to be driven by the capacity of the landscape to store the water intermittently supplied by rainfall and snowmelt such that it is available for transpiration by vegetation at other times. The second is to consider the catchment sensitivity function, which expresses the capacity of the landscape to store and later release water as streamflow. This relationship is also well studied and has been hypothesized to arise from the coevolved architecture of the critical zone. How that coevolution might occur is considerably less well understood relative to the Budyko case,

though some mechanisms have been suggested for basaltic landscapes (Jefferson et al., 2010). Finally, we will examine an intriguing point of overlap between these two perspectives: the relationship between the seasonality of the water balance drivers and the range of hydraulic storage revealed by the catchment sensitivity function.

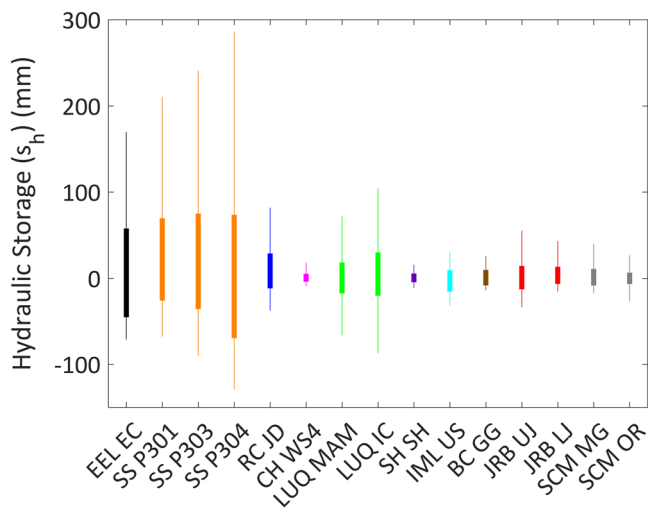


Figure 10. Median-adjusted boxplots summarizing hydraulic storage frequency distributions at 15 CZO catchments. Boxes span the interquartile range and vertical lines show the distribution extent.

6.1. Annual Water Balance Partitioning

Annual water balance dynamics can be examined through the Budyko framework, where observed relationships between climatic aridity, AI , are plotted against evaporative partitioning (approximated here as $1 - Q/P$) (Figure 5). The Budyko relationship has been used to describe the annual water balance of many catchments throughout the world (Budyko, 1974; Gentine et al., 2012). The relationship is believed to arise from a coevolution of climate and critical zone properties, particularly vegetation and soil characteristics (Troch et al., 2013). That is, catchment vegetation evolves with climate to utilize the largest sustainable fraction of soil moisture supplied by infiltration (Eagleson, 1982; Gao et al., 2014; Horton, 1933).

Most of the CZO catchments fall close to the Budyko curve (12 of 15 are within 20%), but others do not. Mean annual water balances at three

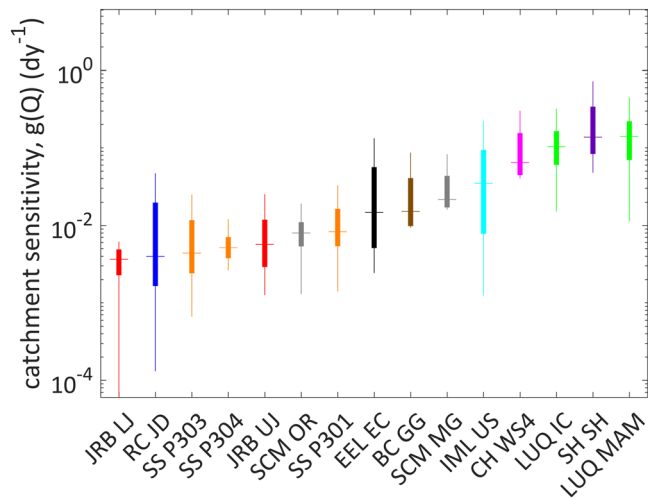


Figure 11. Catchment sensitivity, $g(Q)$, describes the sensitivity of runoff to changes in hydraulic storage state. Boxplots summarize the operational distributions of catchment sensitivity at 15 CZO catchments. Horizontal lines indicate median $g(Q)$ values and sites are ranked left to right by median $g(Q)$. Boxes indicate the interquartile range and vertical lines indicate distribution extents.

sites (SH SH, EEL EC, and SCM MG) plot below Budyko's curve in Figure 5. The most arid catchment, SCM MG, exhibits annual and interannual water balances that fall below Budyko's curve. In June 2003, nearly half of the SCM MG catchment burned during the Aspen Fire (Canfield et al., 2005). Since the fire, which predated observations, vegetation has been undergoing successive phases of recovery (P. Troch and J. Chorover, personal communication, February 8, 2018). The apparent overproduction of runoff relative to Budyko's hypothesis may be due to a disturbance-induced long-term disequilibrium between climate and vegetation.

Elder Creek at the Eel River CZO also exhibits an overproduction of runoff relative to Budyko's hypothesis. The climate at EEL EC is strongly Mediterranean ($\phi = -1.06$, Table 2), where surface water input and evaporative demand are out of phase. Several studies have attributed Budyko anomalies to climatic seasonality (e.g., Berghuijs et al., 2014; Sankarasubramanian & Vogel, 2003), which may also explain the annual inefficiency of plant water use at EEL EC. Because 100% of the precipitation falls as rain, the subsurface is the only storage reservoir capable of seasonally retaining water between the wet winter and dry summer seasons. As shown by Rempe and Dietrich (2018), subsurface storage is filled during the wet season and then vegetation draws from storage throughout the relatively dry growing season to sustain productivity. Perhaps subsurface storage deficits in the dry season impose a seasonal water limitation on vegetation, resulting in relatively inefficient water use compared to other catchments of similar aridity (e.g., SH or SS), where growing season storage does not limit plant water use.

The Shale Hills catchment (SH SH) also exhibits annual and interannual departures from Budyko's hypothesis. This may be attributed to the dominance of shallow subsurface flow paths in streamflow generation (Jin et al., 2011; Li et al., 2017; Lin, 2006). Shallow subsurface flow, or interflow, occurs through a highly fractured zone in the upper 5–8 m of regolith (Sullivan et al., 2016). This fractured zone overlies less fractured

surface storage deficits in the dry season impose a seasonal water limitation on vegetation, resulting in relatively inefficient water use compared to other catchments of similar aridity (e.g., SH or SS), where growing season storage does not limit plant water use.

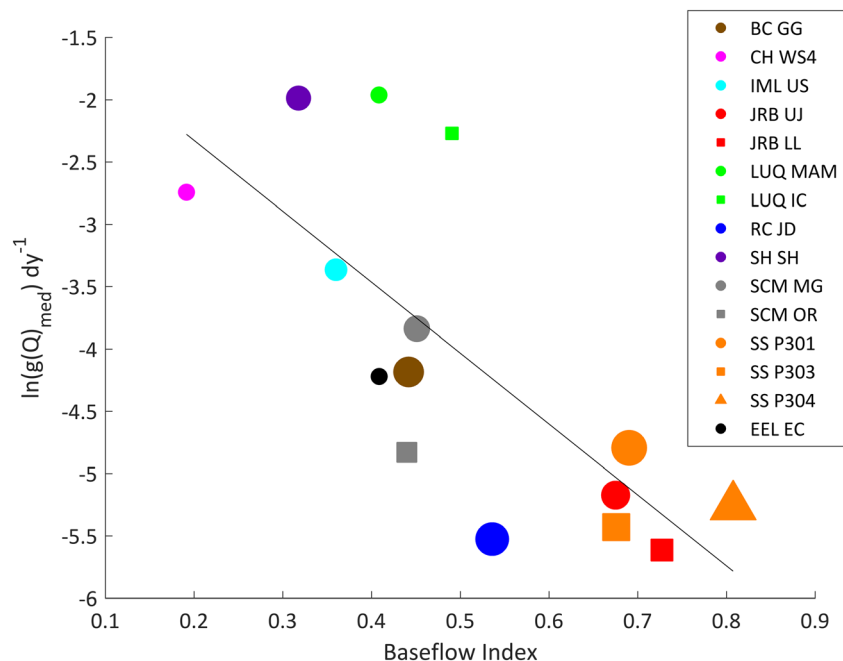


Figure 12. Median catchment sensitivity is negatively related to baseflow index ($p < 0.01$, $R^2 = 0.55$). The size of each marker is scaled by the average annual fraction of precipitation falling as snow at each site (Table 2).

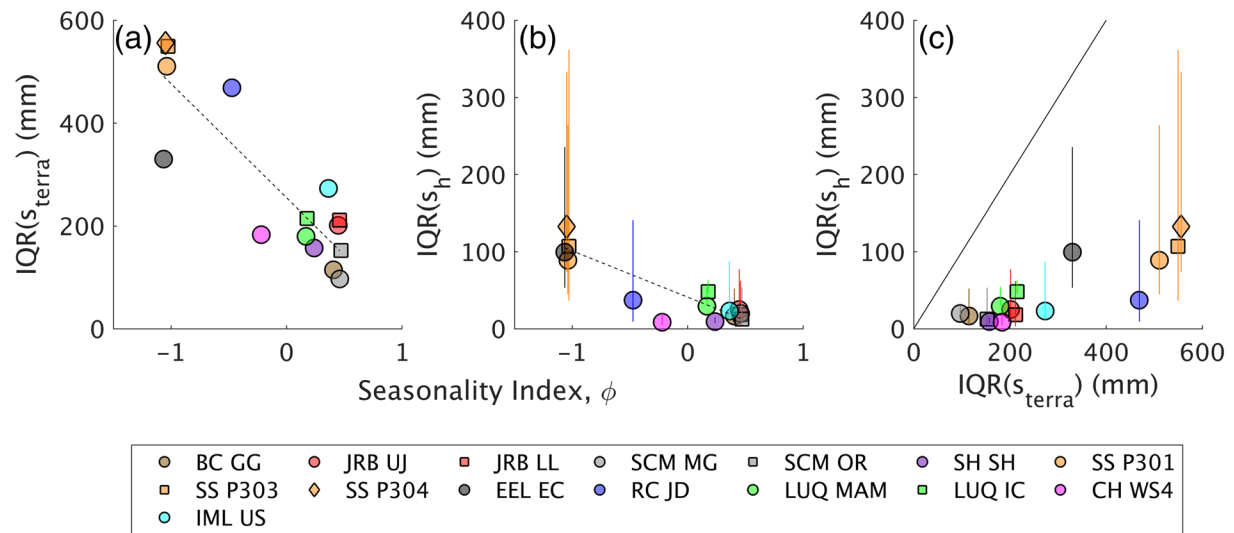


Figure 13. Terrestrial (a) and hydraulic (b) storage interquartile range (IQR) is negatively related to seasonality index ($p << 0.01$). Mediterranean-type climates ($\phi < 0$) exhibit a wider range of dynamic storage states than continental, tropical, or monsoonal-type climates ($\phi > 0$). Vertical error bars of hydraulic storage IQR markers indicate the uncertainty associated with ET fluxes from hydraulic storage zones. The upper extent of error bars assumes that all ET is drawn from hydraulic storage zones (i.e., $\alpha = 1$) and the lower extent of error bars assume that no ET is drawn from hydraulic storage zones (i.e., $\alpha = 0$). (c) Terrestrial and hydraulic storage interquartile ranges are positively related ($p << 0.01$).

rock, upon which an annually persistent perched water table develops and drives interflow. The rapid transmission of meteoric water to the stream via shallow interflow poses a possible explanation for the Budyko anomaly at Shale Hills. Supporting this notion, Troch et al. (2013) showed that short subsurface residence times tend to be associated with lower values of the evaporative index than would be expected from Budyko's hypothesis.

The Calhoun CZO site, CH WS4, does not depart significantly from Budyko's hypothesis in Figure 5. A prominent Bt horizon at CH WS4 (and other catchments throughout the Carolina Piedmont) promotes lateral interflow through shallow transiently perched aquifers. Additionally, the agricultural legacy along the South Carolina Piedmont has led to substantial erosion and a top-down decapitation of the A horizon. The reduced A horizon storage capacity, and associated brief residence times in the perched aquifer, would seem to favor runoff partitioning and non-Budyko behavior (Troch et al., 2013), yet this is not necessarily observed. Currently, our ability to elucidate interannual and intra-annual hydrologic partitioning at the Calhoun CZO is limited by a relatively short discharge record of two water years. As the record continues to accrue and ongoing research matures, our hydrologic picture of this system will sharpen.

Our quantification and interpretation of annual water balance is obscured in part by uncertainties in P and Q . We did not conduct an uncertainty analysis on the Q or P data reported by each CZO. Uncertainties in streamflow arise from uncertainties in stage discharge rating curves, discharge measurement error, and stage measurement error. Uncertainties in P arise from gauge under catch and inaccurate spatial extrapolation of precipitation quantities between gauges in a catchment. In the context of the Budyko plotting space, overestimates in discharge would cause underestimates in the evaporative index and vice versa. Conversely, overestimates in precipitation would cause underestimates in the evaporative index and vice versa. Most of the discharge data provided by the CZOs do not include error estimates, yielding another synthesis opportunity for future cross-CZO investigations. Similarly, the relatively simple scheme used to approximate catchment-wide effective precipitation rates from discrete gauges leaves much room for improvement.

The small size of most CZO catchments relative to those studied by Budyko also obscures our interpretation of the annual water balance. In very large catchments, net groundwater inflows and outflows are likely to be a smaller portion of the long-term annual water balance (Fan, 2019). However, in geologically complex small catchments, like most of the catchments considered here, net groundwater flows likely play a larger role. We ignored net groundwater flows from the annual water balance for convenience and must consider the consequence of this simplification on our understanding of catchment water balances.

Ignoring groundwater import/export biases water balance-derived estimates of annual evapotranspiration. If a catchment is leaky (net groundwater exporter), ET will be overestimated by a simplified water balance framework. Many of the catchments studied here are likely to be leaky, which would cause an overestimation of actual ET and $1 - Q/P$. Indeed, the water balance-derived ET estimates are consistently greater than literature-derived ET values, most of which are based on surface energy balance investigations (Table 2). Annual average ET estimates derived from water balances exceeded literature-derived estimates by as much as 80% and 35% on average (Table 2). This discrepancy may be driven by either groundwater leakage or groundwater storage that is active on longer timescales than can be detected from the relatively short records at each site. Additional synthesis of interbasin groundwater flows and storage is necessary to reduce the uncertainty of annual water balance partitioning in these catchments.

Indeed, ignoring groundwater leakage obscures the plotting positions of each site in Figure 5, such that the plotting distance below Budyko's hypothesis is likely underestimated in our investigation. So, while ignoring groundwater exports causes a high bias in our annual ET estimates, it does not discount the observation that SH SH, EEL EC, and SCM MG seem to overproduce runoff, relative to Budyko's hypothesis.

The water balance analysis presented here is further limited by the relatively short record lengths available at the CZOs. Other studies utilizing the Budyko framework typically consider catchments with at least 50 years of data because over sufficiently long periods, changes in catchment storage are assumed to be negligible, and $ET \approx P - Q$ (assuming groundwater flows are negligible). To better understand similarities and differences in annual partitioning behavior across the CZO network, it is necessary to (1) develop longer records by continuing the collection of runoff and precipitation data and/or (2) leverage ancillary data sets, such as soil moisture or groundwater depth, to approximate changes in catchment storage and groundwater import/export.

6.2. Hydraulic Response and Critical Zone Architecture

We observed a significant negative relationship between catchment sensitivity and baseflow index (Figure 12). According to this result, CZO catchments may be conceptually organized between two contrasting end-members: (1) baseflow dominated with low runoff sensitivity to storage and (2) storm flow dominated with high runoff sensitivity to storage.

Prior studies have attributed catchment hydraulic response to critical zone architecture and regolith development. Notably, Jefferson et al. (2010), Lohse and Dietrich (2005), and Yoshida and Troch (2016) conducted controlled experiments across chronosequences of basaltic catchments. Results showed that baseflow is less dominant in catchments with more developed regolith because extensive primary mineral weathering facilitates the development of clay lenses, favoring shallow interflow (storm flow) over deeper baseflow. Along these same lines, Brantley et al. (2017) used a coupled hydrologic and reactive transport model to illustrate how saturated lateral flow paths can develop at geochemical reaction fronts in a way that allows reaction fronts of minerals of different solubilities to coexist in a steady-state critical zone profile (Harman & Cosans, 2019). Their model suggested that baseflow emanates from deep water tables developed at reaction fronts delineating the interface between unweathered and weathered bedrock. Similarly, interflow emanates from perched water tables atop shallower secondary reaction fronts, usually associated with argillic horizons or the interface between soil and saprolite.

The hydraulic response of CZO catchments observed in this study does appear to be linked to the architecture of the critical zone. Catchments with clay-rich mobile regolith that might divert water laterally prior to reaching the deeper bedrock exhibit less baseflow and higher $g(Q)_{med}$ than catchments with more permeable regoliths that allow for recharge to the bedrock. This is not to say that the architecture of the deeper critical zone is not relevant for understanding the hydraulics, only that a first-order control on baseflow variability is whether the properties of the surficial regolith permit temporally variable recharge to that deeper zone.

To better articulate this hypothesis, regolith profiles for each U.S. CZO site were assembled using a range of available data, including the deep local site knowledge available at each CZO (Figure 14). These profiles are necessarily gross simplifications of the true complexity of each site, but they capture some essential differences between the sites. Profiles are organized from left to right according to baseflow index and $g(Q)_{med}$.

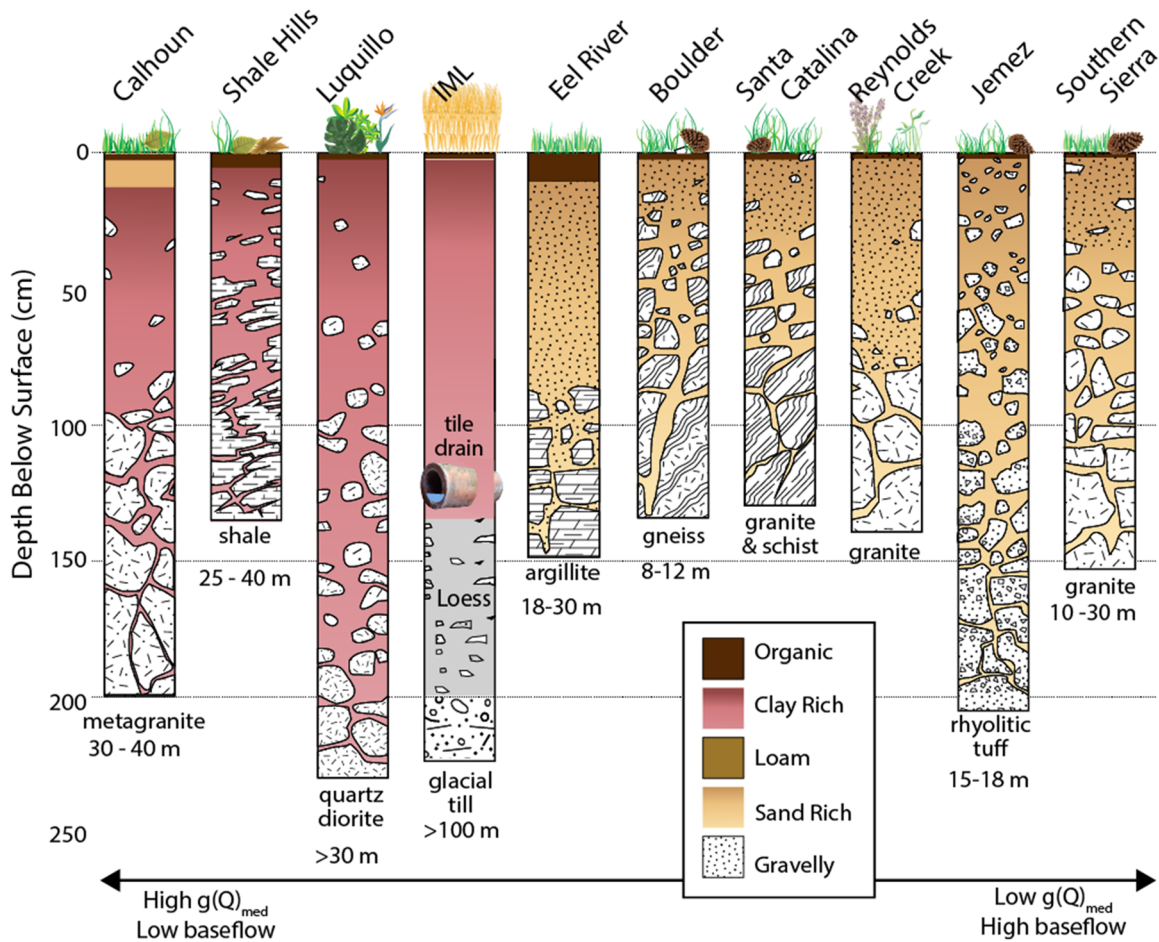


Figure 14. Soil depth and texture profiles for each CZO site. Initial profiles were created following data obtained from the NRCS Web Soil Survey for all sites except Santa Catalina, where no information was available. Each profile was modified based on additional soil information provided by investigators at each site and peer-reviewed literature. The soil texture and depth profile at Santa Catalina were synthesized from information in Holleran et al. (2015). Results at Elder Creek are best explained by storage dynamics in deeper weathered bedrock not pictured above, as detailed in Hahm et al. (2019) and Rempe and Dietrich (2018). Figure design by E. Parrish.

Sites that exhibit the low baseflow indices and high $g(Q)_{med}$ also have structural attributes that favor rapid lateral water transmission as interflow and precipitation regime dominated by rainfall. Calhoun and Luquillo CZOs are both deeply weathered with well-developed regolith and prominent clay horizons (Buss et al., 2013; Orlando et al., 2016; St. Clair et al., 2015). The clay-rich Bt horizon (Calabrese et al., 2018) at CH WS4 may facilitate perched water table development and interflow, though this has not been directly observed. However, Zimmer and McGlynn (2017) observed interflow from perched water tables developed atop clay horizons at another site in the North Carolina Piedmont with similar soil characteristics. At LUQ, hydraulic conductivity decreases sharply at the interface of the surficial organic horizon and clay-rich A horizon in the Mameyes watershed (Schellekens et al., 2004). This permeability contrast cues the development of perched water tables and interflow through shallow organic soils (Schellekens et al., 2004). Both CH and LUQ receive nearly 100% of precipitation as rainfall. At SH, interflow responsible for the majority of runoff generation occurs through highly fractured shale at depths of 5–8 m (Sullivan et al., 2016). Additionally, flow through macropores in channery shale soils at SH is also understood to contribute to runoff generation (Lin, 2006). At SH, between 63% and 82% of the precipitation falls as rain.

The Upper Sangamon basin at the Intensively Managed Landscape (IML) CZO also exhibits low baseflow and high $g(Q)_{med}$; however, unique from other CZOs, anthropogenic manipulation of the critical zone likely plays an important role in controlling basin-wide hydraulic response. European settlement across the Midwestern United States throughout the 19th and 20th centuries prompted drastic changes in landscape

morphology to alleviate poor drainage conditions on fertile agricultural lands. In particular, streams were straightened and widened, and channel networks were extended further into the headwaters (Rhoads et al., 2016). Additionally, tile drains were installed in the shallow subsurface to lower water tables, drain the rooting zone after storms, and reduce surface ponding in low-lying areas (Hewes & Frandson, 1952; Schilling & Helmers, 2008). These human modifications promote the rapid transport of water through and across the landscape by artificially modifying drainage regimes and accelerating transit times (Kumar et al., 2018). However, it remains difficult to establish a causal linkage between anthropogenic impacts and hydraulic response in this study, because the CZO network lacks an un-impacted Midwestern catchment for comparison. Similar to other catchments characterized by low baseflow and high $g(Q)_{med}$ (SH, LUQ, and CH), 74–90% of annual precipitation falls as rain (Table S3).

Two CZO sites, SS and JRB, stand out as being baseflow dominated (baseflow index > 60%) with relatively low $g(Q)_{med}$, compared to other CZO sites (Figure 12). At JRB UJ and LJ, stream flow is primarily fed by groundwater emanating from fractured bedrock (Olshansky et al., 2018; Zapata-Rios et al., 2016), and ~41–63% of annual precipitation falls as snow (McIntosh et al., 2017). Stable isotope data indicate that snowmelt is the dominant source of water to groundwater reservoirs, which are the dominant source of streamflow generation (Liu et al., 2008). During the relatively brief wet season following snowmelt at JRB, interflow through perched aquifers atop clay-rich lenses can also contribute to stream flow (McIntosh et al., 2017); however, annual contributions are dominated by flow from fractured bedrock 15–18 m beneath the surface. Similarly, at SS, groundwater is a key source of runoff, accounting for 61–69% of total streamflow in the Providence Creek subcatchments (P301, P303, and P304) according to the results of a geochemical mixing analysis (Liu et al., 2013). Snow is a critical water subsidy to Providence Creek, accounting for 35–60% of annual precipitation (Hunsaker et al., 2012). In these catchments, both snowmelt and rainfall rapidly infiltrate vertically through well-drained sandy regolith to an aquifer oriented atop fresh bedrock, which is responsible for generating the majority of runoff (Bales et al., 2011; Liu et al., 2013). Moreover, regolith depth exhibits strong lateral variability over short spatial scales throughout Providence Creek (Holbrook et al., 2014), invoking the possible control of fill and spill dynamics on runoff generation (Tromp-van Meerveld & McDonnell, 2006).

Four CZOs (EEL, BC, SCM, and RC) cluster in the middle of the baseflow index and $g(Q)_{med}$ space (Figure 12). Three of these four sites (BC, SCM, and RC) are architecturally and climatically similar. These sites have metamorphic and igneous parent materials (Table 1) and are thinly weathered, with mobile regolith thickness less than 2.4 m (Foster et al., 2015; Holleran et al., 2015; Patton et al., 2018; Pelletier & Rasmussen, 2009). Moreover, these sites receive approximately similar annual quantities of precipitation as snow and rain, with snowfall accounting for 23% to 68% of annual precipitation across sites. End-member mixing analysis at BC GG and SCM MG reveals that the majority of runoff is geochemically similar to precipitation, with precipitation contributing 69% of runoff at BC GG (Cowie et al., 2017) and 51–60% of runoff at SCM MG (Dwivedi et al., 2018). Consistent with this, end-member mixing analysis in a headwater catchment at RC indicates that groundwater averages 25% of annual streamflow, snowmelt 50%, and water traveling along the saprolite/bedrock boundary 25%. These results indicate that runoff may be predominantly generated via shallow subsurface flow paths through saprolite above weathered bedrock (Radke et al., 2019). Indeed, hillslope observations at SCM MG confirm that runoff generation is tightly coupled to the development of a perched water table atop shallow fractured bedrock (Heidbüchel et al., 2013). Limited data are available at BC GG and RC JD for identifying specific runoff generating pathways, an opportunity for future research.

Elder Creek at the Eel River CZO (EEL EC) stands out from other sites clustered in the middle of the baseflow index and $g(Q)_{med}$ space (Figure 12). Unlike the other three catchments in this cohort, EEL EC is more deeply weathered (>20 m to fresh bedrock beneath ridgetops) and receives 100% of precipitation as rain (Hahm et al., 2019). Detailed observations on critical zone architecture and water storage reveal that runoff is primarily generated by deep groundwater flow (Kim et al., 2017; Rempe & Dietrich, 2018). The groundwater table in EEL EC resides within a fractured and weathered bedrock on top of a fresh bedrock boundary and exhibits seasonal vertical variations of 4–6 m (Kim et al., 2017; Rempe & Dietrich, 2018). Groundwater is seasonally recharged during wet winter months by infiltration through a deep vadose zone, once soil and rock moisture storages reach field capacity (Dralle et al., 2018). Given the clear dominance of deep

(>10 m) groundwater in generating streamflow, it is counterintuitive that basin-scale analysis reveals a moderate baseflow index and $g(Q)_{med}$, relative to other CZO catchments. However, during the wet season (winter and spring), the water table is high and in a very transmissive layer of fractured and weathered rock (Salve et al., 2012). As such, shallow groundwater contributions manifest as a flashy streamflow response and may not be interpreted as baseflow by the simple digital filter approach used for baseflow separation.

Regolith depth (depth to bedrock) does not seem to control catchment hydraulic response dynamics. Catchments with similar regolith depths exhibit contrasting hydraulic response metrics (baseflow index and $g(Q)_{med}$). For example, JRB UJ and LJ, EEL EC, and CH WS4 may all be considered deeply weathered, with fresh bedrock residing more than 20 m beneath ridgetops (Table 1). Nevertheless, these sites exhibit contrasting hydraulic response metrics (Figure 12). This observation suggests that catchment storage states and more nuanced regolith properties, such as texture, permeability contrasts, or fracture properties, may exert a stronger control on catchment hydraulic regimes than regolith depth (depth to bedrock) alone. However, exceptions to this observation exist. Hahm et al. (2019) illustrate how regolith depth limits storage capacity into neighboring watersheds underlain by contrasting lithologies in coastal Northern California.

The fraction of precipitation falling as snow also seems to be related to the emergent hydrologic response dynamics of the watersheds considered in this study. Snow-dominated catchments exhibit lower runoff sensitivities to storage and higher baseflow indices, than catchments where the majority of precipitation falls as rain (Figure 12). This observation is in agreement with Barnhart et al. (2016), who observed that seasonal snow melt can bring soils to field capacity and facilitate deep critical zone recharge that drains to streams as baseflow. Moreover, this result is corroborated by Knoben et al. (2018), who argue that the fraction of precipitation falling as snow is one of three climate indices that control global variations in hydrologic responses.

Looking to the future, a shift in winter precipitation phase from snow to rain under future climate scenarios is predicted to occur at many of the U.S. CZOs, especially RC, BC, SS, and JRB (Klos et al., 2014). Results from this study suggest that changing precipitation phase may prompt changes in a catchment's hydrologic signatures, such as the shape of recession curves, the dynamic range of storage, and the baseflow index.

The hypothesized linkage between regolith development and catchment hydraulic response is appealing because it implies a coevolutionary link between catchment form and function. That is, the transmission of water through soils and regolith is both essential to critical zone evolution and a manifestation of the unique historical pathway of such evolution. The hydraulic response metrics quantified in this manuscript (catchment sensitivity and baseflow index) provide an elusive critical zone pattern begging for a unifying explanation. The critical zone community seeks to use emergent patterns in hydrologic behavior among watersheds to infer historical pathways of critical zone evolution. Future work might explore this challenge by deducing the emergent hydrological properties associated with different pathways of critical zone evolution (Riebe et al., 2017).

6.3. Seasonality Explains Dynamic Storage Range

The results suggest that hydroclimatic seasonality partially explains the dynamic storage ranges of CZO catchments. The IQR of s_{terr} and s_h is significantly related to seasonality index, ϕ (Figure 13). At sites where SWI and PET are strongly out of phase, such as SS and EEL, s_{terr} and s_h exhibit large dynamic ranges as storage is progressively filled during the wet season and gradually drained during the dry season. In contrast, at sites where SWI and PET are in phase, such as at JRB and SCM, dynamic ranges of s_{terr} and s_h are small because storage filling and spilling occur at the same time.

We also observed that the dynamic range of s_h was smaller than s_{terr} (Figure 13c), suggesting that hydraulically relevant storage is a subset of total storage. This result corroborates Dralle et al. (2018), who attribute the disparity between hydraulic (direct) and total storage to rock moisture at EEL EC. This result also aligns with the definitions of perceptual catchment storage put forth by Staudinger et al. (2017), who define “dynamic storage” as that which controls streamflow dynamics (what we consider to be s_h) and “extended dynamic storage” as that which controls all catchment fluxes (what we consider to be s_{terr}). Staudinger et al.'s use of the prefix “extended” implies that s_h is only a subset of s_{terr} . Clearly, there remains to be an established textbook lexicon for discussing storage.

The relationship between hydroclimatic seasonality and dynamic storage ranges is somewhat unsurprising since dynamic storage accumulation (and depletion) should depend on the timing and magnitude of terrestrial water inputs and atmospheric water demands. However, the range of dynamic and hydraulic storage also depends on the rate of release of that accumulated storage as streamflow. If the rate of release is fast enough, the range of hydraulic storage will depend only on the ability of individual storms to recharge the hydraulically connected pore space, which will be largely depleted again before the next storm. This can be seen at the IML US where tile drainage likely limits the range of hydraulic storage. Where the release of water is slow, storage can accumulate over multiple years and the range of hydraulic storage ought to be better explained by interannual variability, rather than intra-annual.

Here, the seasonality is likely the primary control on s_h largely because for most of the catchments, and for most of the time, the sensitivity function has a value between $g(Q) = 1/\text{week}$ and $g(Q) = 1/\text{year}$ (Figure 11). That is still a wide range of variability, but not as wide as it could be given that hydraulic conductivity (which idealized analytical models suggest ought to be a primary control on streamflow recession; Brutsaert & Nieber, 1977) varies over 14 orders of magnitude.

This raises two questions: (1) why do catchments tend to have sensitivity functions between 1/week and 1/year? And (2) what determines the variability between catchments within that range? From a mechanistic “Newtonian” point of view, the answer lies in the physical properties of the landscapes. But from a geological point of view, the answer could lie in the explanation for why those properties arise as emergent phenomena that modulate the climatic drivers with coevolutionary feedbacks between hydrologic dynamics and critical zone architecture.

7. Conclusions

This is the first meta-analysis of the commonly observed hydrologic data sets across the CZO network. The implicit hypothesis of this network was that studying the CZ in its entirety at each location would yield insights about form, function, and dynamics. Here, we started the process of extracting quantitative signatures of water storage, partitioning, and release and used these to compare CZO sites. We then drew on the deep accumulated understanding developed at these sites to examine how these patterns could be explained by the critical zone architecture.

The data compiled for this study should propel others forward in drawing on the depth of knowledge amassed at the CZOs. Although the water balance accounting models used here are simple, the time needed to collate them was significant, and we only made a first step in synthesis. More work is needed to synthesize these data and calculate signatures of hydrologic behavior that can be compared across the sites. Metrics of water balance partitioning and catchment hydraulics were chosen in part because they allowed us to focus on the critical role of hydrologic storage as a modulator of hydrologic variability and as a capacity of the landscape that arises from the evolved architecture of the critical zone.

While aridity is a first-order control on evaporative partitioning across the network, seasonality, disturbance, and other factors may drive sites away from the idealized Budyko relationship. Twelve of 15 catchments closely follow Budyko's hypothesis, suggesting a coevolved equilibrium between climate, soils, and vegetative water use at these sites. The remaining catchments produce more runoff than is predicted by Budyko, perhaps suggesting ecohydrological disequilibrium. Catchment sensitivity functions (i.e., storage-discharge relationship), hydraulic storage, and baseflow indices were derived and used as a basis for hydraulic comparison. We observed a negative relationship between baseflow index and catchment sensitivity. Hydroclimatic seasonality and climatic variability appear to explain most of the variation in dynamic storage range between catchments, as well as a substantial portion of the variation in hydraulically connected storage range. Catchments with Mediterranean-type hydroclimates exhibit large dynamic storage ranges, whereas catchments with monsoonal-type hydroclimates exhibit small dynamic storage ranges.

While this pattern may seem to suggest the dominance of climate controls over landscape structure, we believe this is misleading—we propose that the resonance between catchment storage and seasonal dynamics is only possible because of the capacity of the landscape to store and shed water over similar timescales.

It remains to be seen whether this and other hydrologic properties of the landscape can be understood in terms of the coevolution of critical zone architecture, but patterns did emerge from the intersite comparison that suggest this is possible. Catchments with low baseflow indices and high catchment sensitivity receive the majority of precipitation as rain and contain clay-rich regolith profiles, prominent argillic horizons, and/or anthropogenic modifications. On the other hand, sites with high baseflow indices and low catchment sensitivity receive a large portion of precipitation as snow, have more permeable regolith profiles, and range from deeply to thinly weathered.

Data Availability Statement

Data products derived from these parent data sets have been made available through a CUAHSI HydroShare data resource (Wlostowski, A., N. Molotch, C. Harman (2021). CZO Network water budget data products, HydroShare, <https://doi.org/10.4211/hs.29e2ec85770b42c881ef075069646>).

Acknowledgments

Much of the data used in this study were provided by sites within the U.S. Critical Zone Observatory (CZO) network, each of which are funded by the U.S. National Science Foundation: Boulder Creek (grant number EAR-1331828), Shale Hills (grant number EAR-1331726), Eel River (grant number EAR-1331940), Reynolds Creek (grant number EAR-1331872), Southern Sierra (grant number EAR-1331939), Catalina-Jemez (grant number EAR-1331408), intensively managed landscapes (grant number EAR-1331906), Calhoun (grant number EAR-1331846), and Luquillo (grant number EAR-1331841). The Pacific Southwest Research Station, USDA Forest Service, which operates the Kings River Experimental Watersheds, and the Sierra National Forest, provided additional data and support at the Southern Sierra CZO. The USDA Reynolds Creek Experimental Watershed provided additional data and support at the Reynolds Creek CZO. Additional monetary support for this research was graciously provided by Timothy White, through National Science Foundation grant number ICER-1445246. Acknowledgement and citation for the parent data sets used in this study are provided within the main text and the supporting information.

References

- Addor, N., Nearing, G., Prieto, C., Newman, A. J., Le Vine, N., & Clark, M. P. (2018). A ranking of hydrological signatures based on their predictability in space. *Water Resources Research*, *54*, 8792–8812. <https://doi.org/10.1029/2018WR022606>
- Addor, N., Newman, A. J., Mizukami, N., & Clark, M. P. (2017). The CAMELS data set: Catchment attributes and meteorology for large-sample studies. *Hydrology and Earth System Sciences*, *21*, 5293–5313. <https://doi.org/10.5065/D6MW2F4D>
- Anderson, E. (2006). Snow accumulation and ablation model—SNOW-17. Retrieved from http://www.nws.noaa.gov/oh/hrl/nwsrfs/users_manual/part2/_pdf/22snow17.pdf
- Arnold, J. G., & Allen, P. M. (1999). Automated methods for estimating baseflow and ground water recharge from streamflow records 1. *Journal of the American Water Resources Association*, *35*(2), 411–424. <https://doi.org/10.1111/j.1752-1688.1999.tb03599.x>
- Bales, R. C., Goulden, M. L., Hunsaker, C. T., Conklin, M. H., Hartsough, P. C., O'Geen, A. T., et al. (2018). Mechanisms controlling the impact of multi-year drought on mountain hydrology. *Scientific Reports*, *8*, 690. <https://doi.org/10.1038/s41598-017-19007-0>
- Bales, R. C., Hopmans, J. W., O'Geen, A. T., Meadows, M., Hartsough, P. C., Kirchner, P., et al. (2011). Soil moisture response to snowmelt and rainfall in a Sierra Nevada mixed-conifer forest. *Vadose Zone Journal*, *10*(3), 786–799. <https://doi.org/10.2136/vzj2011.0001>
- Bales, R. C., Molotch, N. P., Painter, T. H., Dettinger, M. D., Rice, R., & Dozier, J. (2006). Mountain hydrology of the western United States. *Water Resources Research*, *42*, W08432. <https://doi.org/10.1029/2005WR004387>
- Barnhart, T. B., Molotch, N. P., Livneh, B., Harpold, A. A., Knowles, J. F., & Schneider, D. (2016). Snowmelt rate dictates streamflow. *Geophysical Research Letters*, *43*, 8006–8016. <https://doi.org/10.1002/2016GL069690>
- Bart, R., & Hope, A. (2014). Inter-seasonal variability in baseflow recession rates: The role of aquifer antecedent storage in Central California watersheds. *Journal of Hydrology*, *519*, 205–213. <https://doi.org/10.1016/j.jhydrol.2014.07.020>
- Befus, K. M., Sheehan, A. F., Leopold, M., Anderson, S. P., & Anderson, R. S. (2011). Seismic constraints on critical zone architecture, Boulder Creek watershed, Front Range, Colorado. *Vadose Zone Journal*, *10*, 915–927. <https://doi.org/10.2136/vzj2010.0108>
- Berghuijs, W. R., Hartmann, A., & Woods, R. A. (2016). Streamflow sensitivity to water storage changes across Europe. *Geophysical Research Letters*, *43*, 1980–1987. <https://doi.org/10.1002/2016GL067927>
- Berghuijs, W. R., Sivapalan, M., Woods, R. A., & Savenije, H. H. (2014). Patterns of similarity of seasonal water balances: A window into streamflow variability over a range of time scales. *Water Resources Research*, *50*, 5638–5661. <https://doi.org/10.1002/2014WR015692>
- Received
- Beven, K., Wood, E. F., & Sivapalan, M. (1988). On hydrological heterogeneity—Catchment morphology and catchment response. *Journal of Hydrology*, *100*, 353–375. [https://doi.org/10.1016/0022-1694\(88\)90192-8](https://doi.org/10.1016/0022-1694(88)90192-8)
- Black, P. E. (1997). Watershed functions. *JAWRA Journal of the American Water Resources Association*, *33*(1), 1–11. <https://doi.org/10.1111/j.1752-1688.1997.tb04077.x>
- Brantley, S. L., DiBiase, R. A., Russo, T. A., Shi, Y., Lin, H., Davis, K. J., et al. (2016). Designing a suite of measurements to understand the critical zone. *Earth Surface Dynamics*, *4*(1), 211–235. <https://doi.org/10.5194/esurf-4-211-2016>
- Brantley, S. L., Goldhaber, M. B., & Ragnarsdottir, K. V. (2007). Crossing disciplines and scales to understand the critical zone. *Elements*, *3*(5), 307–314. <https://doi.org/10.2113/gselements.3.5.307>
- Brantley, S. L., & Lebedeva, M. (2011). Learning to read the chemistry of regolith to understand the critical zone. *Annual Review of Earth and Planetary Sciences*, *39*(1), 387–416. <https://doi.org/10.1146/annurev-earth-040809-152321>
- Brantley, S. L., Lebedeva, M. I., Balashov, V. N., Singha, K., Sullivan, P. L., & Stinchcomb, G. (2017). Toward a conceptual model relating chemical reaction fronts to water flow paths in hills. *Geomorphology*, *277*, 100–117. <https://doi.org/10.1016/J.GEOMORPH.2016.09.027>
- Brooks, P. D., Chorover, J., Fan, Y., Godsey, S. E., Maxwell, R. M., McNamara, J. P., & Tague, C. (2015). Hydrological partitioning in the critical zone: Recent advances and opportunities for developing transferable understanding of water cycle dynamics. *Water Resources Research*, *51*, 6973–6987. <https://doi.org/10.1002/2015WR017039>
- Brutsaert, W., & Nieber, J. L. (1977). Regionalized drought flow hydrographs from a mature glaciated plateau. *Water Resources Research*, *13*(3), 637–643. <https://doi.org/10.1029/WR013i003p0637>
- Budyko, M. I. (1974). *Climate and life*. New York, NY: Academic Press.
- Buss, H. L., Brantley, S. L., Scatena, F. N., Bazilievskaya, E. A., Blum, A., Schulz, M., et al. (2013). Probing the deep critical zone beneath the Luquillo experimental forest, Puerto Rico. *Earth Surface Processes and Landforms*, *38*(10), 1170–1186. <https://doi.org/10.1002/esp.3409>
- Calabrese, S., Richter, D. D., & Porporato, A. (2018). The formation of clay-enriched horizons by Lessivage. *Geophysical Research Letters*, *45*, 7588–7595. <https://doi.org/10.1029/2018GL078778>
- Canfield, H. E., Goodrich, D. C., & Burns, I. S. (2005). Selection of parameters values to model post-fire runoff and sediment transport at the watershed scale in southwestern forests. Retrieved from www.tucson.ars.ag.gov/agwa/
- Carrer, G. E., Klaus, J., & Pfister, L. (2018). Assessing the catchment storage function through a dual-storage concept. *Water Resources Research*, *55*, 476–494. <https://doi.org/10.1029/2018WR022856>

- Cowie, R. M., Knowles, J. F., Dailey, K. R., Williams, M. W., Mills, T. J., & Molotch, N. P. (2017). Sources of streamflow along a headwater catchment elevational gradient. *Journal of Hydrology*, *549*, 163–178. <https://doi.org/10.1016/j.jhydrol.2017.03.044>
- Davis, K., & Shi, Y. (2019). Ameriflux US-SSH Susquehanna Shale Hills Critical Zone Observatory. <https://doi.org/10.1016/N/A>
- Deal, E., Braun, J., & Botter, G. (2018). Understanding the role of rainfall and hydrology in determining fluvial erosion efficiency. *Journal of Geophysical Research: Earth Surface*, *123*, 744–778. <https://doi.org/10.1002/2017JF004393>
- Dralle, D. N., Jesse Hahm, W., Rempe, D. M., Karst, N. J., Thompson, S. E., & Dietrich, W. E. (2018). Quantification of the seasonal hillslope water storage that does not drive streamflow. *Hydrological Processes*, *32*(13), 1978–1992. <https://doi.org/10.1002/hyp.11627>
- Duan, Q. Y., Gupta, V. K., & Sorooshian, S. (1993). Shuffled complex evolution approach for effective and efficient global minimization. *Journal of Optimization Theory and Applications*, *76*(3), 501–521. <https://doi.org/10.1007/BF00939380>
- Dwivedi, R., Meixner, T., McIntosh, J. C., Ferré, P. A. T., Eastoe, C. J., Niu, G., et al. (2018). Hydrologic functioning of the deep critical zone and contributions to streamflow in a high elevation catchment: Testing of multiple conceptual models. *Hydrological Processes*, *33*(4), 476–494. <https://doi.org/10.1002/hyp.13363>
- Eagleson, P. S. (1982). Ecological optimality in water-limited natural soil-vegetation systems: 1. Theory and hypothesis. *Water Resources Research*, *18*(2), 325–340. <https://doi.org/10.1029/WR018i002p00325>
- Fan, Y. (2019). Are catchments leaky? *WIREs Water*, *6*(6), 1–25. <https://doi.org/10.1002/wat2.1386>
- Field, J. P., Breshears, D. D., Law, D. J., Villegas, J. C., López-Hoffman, L., Brooks, P. D., et al. (2015). Critical zone services: Expanding context, constraints, and currency beyond ecosystem services. *Vadose Zone Journal*, *14*(1), 0. <https://doi.org/10.2136/vzj2014.10.0142>
- Flerchinger, G. N. (2019). AmeriFlux US-Rms RCEW Mountain Big Sagebrush. <https://doi.org/10.17190/AMF/1375202>
- Foster, M. A., Anderson, R. S., Wyshnytzky, C. E., Ouimet, W. B., & Dethier, D. P. (2015). Hillslope lowering rates and mobile-regolith residence times from in situ and meteoric ¹⁰Be analysis, Boulder Creek Critical Zone Observatory, Colorado. *GSA Bulletin*, *127*(5/6), 862–878. <https://doi.org/10.1130/B31115.1>
- Gao, H., Hrachowitz, M., Schymanski, S. J., Fenicia, F., Sriwongsitanon, N., & Savenije, H. H. G. (2014). Climate controls how ecosystems size the root zone storage capacity at catchment scale. *Geophysical Research Letters*, *41*, 7916–7923. <https://doi.org/10.1002/2014GL061668>
- Gentine, P., Odorico, P. D., Lintner, B. R., Sivandran, G., & Salvucci, G. (2012). Interdependence of climate, soil, and vegetation as constrained by the Budyko curve. *Journal of Geophysical Research*, *39*, L19404. <https://doi.org/10.1029/2012GL053492>
- Global Modeling and Assimilation Office (GMAO) (2015a). *MERRA-2 inst1_2d_asm_Nx: 2d,1-Hourly,Instantaneous,Single-Level,Assimilation,Single-Level Diagnostics V5.12.4*. Greenbelt, MD, USA: Goddard Earth Sciences Data and Information Services Center (GES DISC). <https://doi.org/10.5067/3Z173KIE2TPD>
- Global Modeling and Assimilation Office (GMAO) (2015b). *MERRA-2 tavg1_2d_rad_Nx: 2d,1-Hourly,Time-Averaged,Single-Level,Assimilation,Radiation Diagnostics V5.12.4*. Greenbelt, MD, USA: Goddard Earth Sciences Data and Information Services Center (GES DISC). <https://doi.org/10.5067/Q9QMY5PBNV1T>
- Graham, R. C., Rossi, A. M., & Hubbert, K. R. (2010). Rock to regolith conversion: Producing hospitable substrates for terrestrial ecosystems. *GSA Today*, *20*, 4–9. <https://doi.org/10.1130/GSAT57A.1>
- Hahm, W. J., Rempe, D. M., Dralle, D. N., Dawson, T. E., Lovill, S. M., Bryk, A. B., et al. (2019). Lithologically controlled subsurface critical zone thickness and water storage capacity determine regional plant community composition. *Water Resources Research*, *55*, 3028–3055. <https://doi.org/10.1029/2018WR023760>
- Harman, C. J., & Cosans, C. L. (2019). A low dimensional model of bedrock weathering and lateral flow co-evolution in hillslopes: 2. Controls on weathering and permeability profiles, drainage hydraulics and solute export pathways. *Hydrological Processes*, *33*(8), 1168–1190. <https://doi.org/10.1002/hyp.13385>
- Heidbüchel, I., Troch, P. A., & Lyon, S. W. (2013). Separating physical and meteorological controls of variable transit times in zero-order catchments. *Water Resources Research*, *49*, 7644–7657. <https://doi.org/10.1002/2012WR013149>
- Hewes, L., & Frandson, P. E. (1952). Occupying the wet prairie: The role of artificial drainage in Story County, Iowa. *Annals of the Association of American Geographers*, *42*(1), 24–50. <https://doi.org/10.2307/2561045>
- Hock, R. (2003). Temperature index melt modelling in mountain areas. *Journal of Hydrology*, *282*, 104–115. [https://doi.org/10.1016/S0022-1694\(03\)00257-9](https://doi.org/10.1016/S0022-1694(03)00257-9)
- Holbrook, W. S., Marcon, V., Bacon, A. R., Brantley, S. L., Carr, B. J., Flinchum, B. A., et al. (2019). Links between physical and chemical weathering inferred from a 65-m-deep borehole through Earth's critical zone. *Scientific Reports*, *9*, 4495. <https://doi.org/10.1038/s41598-019-40819-9>
- Holbrook, W. S., Riebe, C. S., Elwaseif, M., Hayes, J. L., Basler-Reeder, K. L., Harry, D., et al. (2014). Geophysical constraints on deep weathering and water storage potential in the Southern Sierra Critical Zone Observatory. *Earth Surface Processes and Landforms*, *39*(3), 366–380. <https://doi.org/10.1002/esp.3502>
- Holleran, M., Levi, M., & Rasmussen, C. (2015). Quantifying soil and critical zone variability in a forested catchment through digital soil mapping. *The Soil*, *1*(1), 47–64. <https://doi.org/10.5194/soil-1-47-2015>
- Horton, R. E. (1933). The role of infiltration in the hydrologic cycle. *Transactions of the American Geophysical Union*, *14*(1), 446–460. <https://doi.org/10.1029/TR014i001p00446>
- Hunsaker, C. T., Whitaker, T. W., & Bales, R. C. (2012). Snowmelt runoff and water yield along elevation and temperature gradients in California's Southern Sierra Nevada. *JAWRA Journal of the American Water Resources Association*, *48*(4), 667–678. <https://doi.org/10.1111/j.1752-1688.2012.00641.x>
- Jefferson, A., Grant, G. E., Lewis, S. L., & Lancaster, S. T. (2010). Coevolution of hydrology and topography on a basalt landscape in the Oregon Cascade Range, USA. *Earth Surface Processes and Landforms*, *35*, 803–816. <https://doi.org/10.1002/esp.1976>
- Jefferson, A., Ferrier, K. L., Perron, J. T., & Ramalho, R. (2014). In K. S. Harpp, E. Mittelstaedt, N. D'Ozouville, D. W. Graham (Eds.), *Controls on the hydrological and topographic evolution of shield volcanoes and volcanic ocean islands*. Washington, DC: American Geophysical Union. <https://doi.org/10.1002/9781118852538>
- Jencso, K. G., Meglynn, B. L., Gooseff, M. N., Bencala, K. E., & Wondzell, S. M. (2010). Hillslope hydrologic connectivity controls riparian groundwater turnover: Implications of catchment structure for riparian buffering and stream water sources. *Water Resources Research*, *46*, W10524. <https://doi.org/10.1029/2009WR008818>
- Jenny, H. (1941). *Factors of soil formation: A system of quantitative pedology* (1st ed.). New York: McGraw Hill. Retrieved from. <http://hdl.handle.net/2027/mdp.39015067110372>
- Jin, L., Andrews, D. M., Holmes, G. H., Lin, H., & Brantley, S. L. (2011). Opening the “black box”: Water chemistry reveals hydrological controls on weathering in the Susquehanna Shale Hills Critical Zone Observatory. *Vadose Zone Journal*, *10*(3), 928–942. <https://doi.org/10.2136/vzj2010.0133>

- Kim, H., Dietrich, W. E., Thurnhoffer, B. M., Bishop, J. K. B., & Fung, I. Y. (2017). Controls on solute concentration-discharge relationships revealed by simultaneous hydrochemistry observations of hillslope runoff and stream flow: The importance of critical zone structure. *Water Resources Research*, *53*, 1424–1443. <https://doi.org/10.1002/2016WR019722>
- Kirchner, J. W. (2009). Catchments as simple dynamical systems: Catchment characterization, rainfall-runoff modeling, and doing hydrology backward. *Water Resources Research*, *45*, W02429. <https://doi.org/10.1029/2008WR006912>
- Klos, P. Z., Link, T. E., & Abatzoglou, J. T. (2014). Extent of the rain-snow transition zone in the western U.S. under historic and projected climate. *Geophysical Research Letters*, *41*, 4560–4568. <https://doi.org/10.1002/2014GL060500> Received
- Knoben, W. J. M., Woods, R. A., & Freer, J. E. (2018). A quantitative hydrological climate classification evaluated with independent streamflow data. *Water Resources Research*, *54*, 5088–5109. <https://doi.org/10.1029/2018WR022913>
- Kormos, P. R., Marks, D. G., Seyfried, M. S., Havens, S. C., Hedrick, A., Lohse, K. A., & Sandusky, M. (2017). 31 years of hourly spatially distributed air temperature, humidity, and precipitation amount and phase from Reynolds Critical Zone Observatory. *Earth System Science Data Discussions*, *10*, 1197–1205. <https://doi.org/10.5194/essd-2017-82>
- Krier, R., Matgen, P., Goergen, K., Pfister, L., Hoffmann, L., Kirchner, J. W., et al. (2012). Inferring catchment precipitation by doing hydrology backward: A test in 24 small and mesoscale catchments in Luxembourg. *Water Resources Research*, *48*, W10525. <https://doi.org/10.1029/2011WR010657>
- Kumar, P. (2011). Typology of hydrologic predictability. *Water Resources Research*, *47*, W00H05. <https://doi.org/10.1029/2010WR009769>
- Kumar, P., Le, P. V. V., Papanicolaou, A. N. T., Rhoads, B. L., Anders, A. M., Stumpf, A., et al. (2018). Critical transition in critical zone of intensively managed landscapes. *Anthropocene*, *22*, 10–19. <https://doi.org/10.1016/j.ANCENE.2018.04.002>
- Li, H.-Y., Sivapalan, M., Tian, F., & Harman, C. (2014). Functional approach to exploring climatic and landscape controls of runoff generation: 1. Behavioral constraints on runoff volume. *Water Resources Research*, *50*, 9300–9322. <https://doi.org/10.1002/2014WR016307>
- Li, L., Bao, C., Sullivan, P. L., Brantley, S., Shi, Y., & Duffy, C. (2017). Understanding watershed hydrogeochemistry: 2. Synchronized hydrological and geochemical processes drive stream chemostatic behavior. *Water Resources Research*, *53*, 2346–2367. <https://doi.org/10.1002/2016WR018935>
- Lin, H. (2006). Temporal stability of soil moisture spatial pattern and subsurface preferential flow pathways in the Shale Hills catchment. *Vadose Zone Journal*, *5*, 317–340. <https://doi.org/10.2136/vzj2005.0058>
- Litvak, M. (2019). Ameriflux US-Vcm Valles Caldera Mixed Conifer. <https://doi.org/10.17190/AMF/1246121>
- Liu, F., Hunsaker, C., & Bales, R. C. (2013). Controls of streamflow generation in small catchments across the snow-rain transition in the Southern Sierra Nevada, California. *Hydrological Processes*, *27*(14), 1959–1972. <https://doi.org/10.1002/hyp.9304>
- Liu, F., Parmenter, R., Brooks, P. D., Conklin, M. H., & Bales, R. C. (2008). Seasonal and interannual variation of streamflow pathways and biogeochemical implications in semi-arid, forested catchments in Valles Caldera, New Mexico. *Ecohydrology*, *1*(3), 239–252. <https://doi.org/10.1002/eco.22>
- Lohse, K. A., & Dietrich, W. E. (2005). Contrasting effects of soil development on hydrological properties and flow paths. *Water Resources Research*, *41*, W12419. <https://doi.org/10.1029/2004WR003403>
- Loomis, J., Kent, P., Strange, L., Fausch, K., & Covich, A. (2000). Measuring the total economic value of restoring ecosystem services in an impaired river basin: Results from a contingent valuation survey. *Ecological Economics*, *33*(1), 103–117. [https://doi.org/10.1016/S0921-8009\(99\)00131-7](https://doi.org/10.1016/S0921-8009(99)00131-7)
- Maher, K. (2010). The dependence of chemical weathering rates on fluid residence time. *Earth and Planetary Science Letters*, *294*(1–2), 101–110. <https://doi.org/10.1016/j.epsl.2010.03.010>
- Maher, K. (2011). The role of fluid residence time and topographic scales in determining chemical fluxes from landscapes. *Earth and Planetary Science Letters*, *312*, 48–58. <https://doi.org/10.1016/j.epsl.2011.09.040>
- McIntosh, J. C., Schaumberg, C., Perdrial, J., Harpold, A., Vázquez-Ortega, A., Rasmussen, C., et al. (2017). Geochemical evolution of the critical zone across variable time scales informs concentration-discharge relationships: Jemez River Basin Critical Zone Observatory. *Water Resources Research*, *53*, 4169–4196. <https://doi.org/10.1002/2016WR019712>
- McNamara, J. P., Tetzlaff, D., Bishop, K., Soulsby, C., Seyfried, M., Peters, N. E., et al. (2011). Storage as a metric of catchment comparison. *Hydrological Processes*, *25*(21), 3364–3371. <https://doi.org/10.1002/hyp.8113>
- Meyers, T. (2019). AmeriFlux US-Bo1 Bondville. <https://doi.org/10.17190/AMF/1246036>
- Mitchell, K. E. (2009). In D. Mocko, & NASA/GSFC/HSL (Eds.), *NLDAS Forcing Data L4 Hourly 0.125 × 0.125 degree V001*, Edited by Greenbelt, Maryland, USA: Goddard Earth Sciences Data and Information Services Center (GES DISC). <https://doi.org/10.5067/H3CJY2R7C1RU>
- Monteith, J. L. (1965). Evaporation and environment. *Symposia of the Society for Experimental Biology*, *19*, 205–234.
- Monteith, J. L. (1973). *Principles of environmental physics*. London: Edward Arnold. Retrieved from <http://ucblibraries.summon.serialsolutions.com/2.0.0/link/0/eLvHCXmWY2AwNtlz0EUrE0CnzKUYJ6UmGhmKppkkm5gkPQGb7qApMhMzlwNz8H7nAAuvQEuvSJNgJgYDlJEMUJcRdIRzUWJKPnxtDWj8wsgc2D6wMKwLnmZmYAUWtGbAnMnq5O7j4wruoBsaA4tlcxNTJ16pMfTQHZikGSofdEcyd2ky3F6kusZnKIEFtP9Aii>
- Murphy, S. F., & Stallard, R. F. (2012). Hydrology and climate of four watersheds in eastern Puerto Rico water quality and landscape processes of four watersheds in eastern Puerto Rico. In S. Murphy & R. Stallard (Eds.), *Water quality and landscape processes of four watersheds in eastern Puerto Rico* (pp. 48–83). Reston, VA: U.S. Geological Survey. Retrieved from <https://pubs.usgs.gov/pp/1789/pdfs/ChapterC.pdf>
- Murphy, S. F., Stallard, R. F., Scholl, M. A., Gonzá Lez, G., & Torres-Sá Nchez, A. J. (2017). Reassessing rainfall in the Luquillo Mountains, Puerto Rico: Local and global ecohydrological implications. *PLoS ONE*, *12*, e0180987. <https://doi.org/10.1371/journal.pone.0180987>
- Myneni, R., Knyazikhin, Y., & Park, T. (2015). MCD15A2H MODIS/Terra+Aqua Leaf Area Index/FPAR 8-day L4 Global 500m SIN Grid V006. NASA EOSDIS Land Processes DAAC. <https://doi.org/10.5067/MODIS/MCD15A2H.006>
- Nielson, T. (2017). Application of hydrogeophysical imaging in the Reynolds Creek Critical Zone Observatory. *Boise State University Theses and Dissertations*. Boise State University. <https://doi.org/10.18122/B22X42>
- Olshansky, Y., White, A. M., Moravec, B. G., McIntosh, J., & Chorover, J. (2018). Subsurface pore water contributions to stream concentration-discharge relations across a snowmelt hydrograph. *Frontiers in Earth Science*, *6*, 181. <https://doi.org/10.3389/feart.2018.00181>
- Olyphant, J., Pelletier, J. D., & Johnson, R. (2016). Topographic correlations with soil and regolith thickness from shallow-seismic refraction constraints across upland hillslopes in the Valles Caldera, New Mexico. *Earth Surface Processes and Landforms*, *41*(12), 1684–1696. <https://doi.org/10.1002/esp.3941>

- Orlando, J., Comas, X., Hynek, S. A., Buss, H. L., & Brantley, S. L. (2016). Architecture of the deep critical zone in the Rio Icacos watershed (Luquillo Critical Zone Observatory, Puerto Rico) inferred from drilling and ground penetrating radar (GPR). *Earth Surface Processes and Landforms*, *41*(13), 1826–1840. <https://doi.org/10.1002/esp.3948>
- Patton, N. R., Lohse, K. A., Godsey, S. E., Crosby, B. T., & Seyfried, M. S. (2018). Predicting soil thickness on soil mantled hillslopes. *Nature Communications*, *9*, 3329. <https://doi.org/10.1038/s41467-018-05743-y>
- Payn, R. A., Gooseff, M. N., McGlynn, B. L., Bencala, K. E., & Wondzell, S. M. (2012). Exploring changes in the spatial distribution of stream baseflow generation during a seasonal recession. *Water Resources Research*, *48*, W04519. <https://doi.org/10.1029/2011WR011552>
- Pelletier, J. D., & Rasmussen, C. (2009). Geomorphically based predictive mapping of soil thickness in upland watersheds. *Water Resources Research*, *45*, W09417. <https://doi.org/10.1029/2008WR007319>
- Penman, H. L. (1947). Natural evaporation from open water, bare soil and grass. *Proceedings of the Royal Society of London A: Mathematical Physical and Engineering Sciences*, *193*(1032), 120–145.
- Poff, N. L., Allan, J. D., Bain, M. B., Karr, J. R., Prestegard, K. L., Richter, B. D., et al. (1997). The Natural Flow Regime A paradigm for river conservation and restoration. *Bioscience*, *47*(11), 769–784. <https://doi.org/10.2307/1313099>
- PRISM Climate Group (2019). Gridded Climat Data for the U.S.
- Radke, A. G., Godsey, S. E., Lohse, K. A., McCorkle, E. P., Perdrial, J., Seyfried, M. S., & Holbrook, W. S. (2019). Spatiotemporal heterogeneity of water flowpaths controls dissolved organic carbon sourcing in a snow-dominated, headwater catchment. *Frontiers in Ecology and Evolution*, *7*, 46. <https://doi.org/10.3389/fevo.2019.00046>
- Rempe, D. M., & Dietrich, W. E. (2014). A bottom-up control on fresh-bedrock topography under landscapes. *Proceedings of the National Academy of Sciences*, *111*(18), 6576–6581. <https://doi.org/10.1073/pnas.1404763111>
- Rempe, D. M., & Dietrich, W. E. (2018). Direct observations of rock moisture, a hidden component of the hydrologic cycle. *Proceedings of the National Academy of Sciences*, *115*(11), 2664–2669. <https://doi.org/10.1073/pnas.1800141115>
- Rhoads, B., Lewis, Q. W., & Andresen, W. (2016). Historical changes in channel network extent and channel planform in an intensively managed landscape: Natural versus human-induced effects. *Geomorphology*, *252*, 17–31. <https://doi.org/10.1016/j.geomorph.2015.04.021>
- Riebe, C. S., Hahn, W. J., & Brantley, S. L. (2017). Controls on deep critical zone architecture: A historical review and four testable hypotheses. *Earth Surface Processes and Landforms*, *42*(1), 128–156. <https://doi.org/10.1002/esp.4052>
- Salve, R., Rempe, D. M., & Dietrich, W. E. (2012). Rain, rock moisture dynamics, and the rapid response of perched groundwater in weathered, fractured argillite underlying a steep hillslope. *Water Resources Research*, *48*, 11528. <https://doi.org/10.1029/2012WR012583>
- Sankarasubramanian, A., & Vogel, R. M. (2003). Hydroclimatology of the continental United States. *Geophysical Research Letters*, *30*(7), 1363. <https://doi.org/10.1029/2002GL015937>
- Sawicz, K., Wagener, T., Sivapalan, M., Troch, P. A., & Carrillo, G. (2011). Catchment classification: Empirical analysis of hydrologic similarity based on catchment function in the eastern USA. *Hydrology and Earth System Sciences Discussions*, *8*(3), 4495–4534. <https://doi.org/10.5194/hessd-8-4495-2011>
- Schellekens, J., Scatena, F. N., Bruijnzeel, L. A., van Dijk, A. I. J. M., Groen, M. M. A., & van Hogezaand, R. J. P. (2004). Stormflow generation in a small rainforest catchment in the Luquillo experimental forest, Puerto Rico. *Hydrological Processes*, *18*(3), 505–530. <https://doi.org/10.1002/hyp.1335>
- Schilling, K. E., & Helmers, M. (2008). Effects of subsurface drainage tiles on streamflow in Iowa agricultural watersheds: Exploratory hydrograph analysis. *Hydrological Processes*, *22*(23), 4497–4506. <https://doi.org/10.1002/hyp.7052>
- Shi, Y., Davis, K. J., Duffy, C. J., Yu, X., Shi, Y., Davis, K. J., et al. (2013). Development of a coupled land surface hydrologic model and evaluation at a critical zone observatory. *Journal of Hydrometeorology*, *14*(5), 1401–1420. <https://doi.org/10.1175/JHM-D-12-0145.1>
- Shuttleworth, J. W., & Wallace, J. S. (1985). Evaporation from sparse crops—An energy combination theory. *Quarterly Journal of the Royal Meteorological Society*, *111*(469), 839–855. <https://doi.org/10.1002/qj.49711146910>
- Sivapalan, M., & Blöschl, G. (2017). The growth of hydrological understanding: Technologies, ideas, and societal needs shape the field. *Water Resources Research*, *53*, 8137–8146. <https://doi.org/10.1002/2017WR021396>
- Sivapalan, M., Yaeger, M. A., Harman, C. J., Xu, X., & Troch, P. A. (2011). Functional model of water balance variability at the catchment scale: 1. Evidence of hydrologic similarity and space-time symmetry. *Water Resources Research*, *47*, W02522. <https://doi.org/10.1029/2010WR009568>
- Soil Survey Staff, Natural Resources Conservation Service, U. S. D. of A (2018). Web Soil Survey.
- St. Clair, J., Moon, S., Holbrook, W. S., Perron, J. T., Riebe, C. S., Martel, S. J., et al. (2015). Geophysical imaging reveals topographic stress control of bedrock weathering. *Science*, *350*(6260), 534–538. <https://doi.org/10.1126/science.aab2210>
- Staudinger, M., Stoelzle, M., Seeger, S., Seibert, J., Weiler, M., & Stahl, K. (2017). Catchment water storage variation with elevation. *Hydrological Processes*, *31*(11), 2000–2015. <https://doi.org/10.1002/hyp.11158>
- Stephenson, G. R., & Freeze, R. A. (1974). Mathematical simulation of subsurface flow contributions to snowmelt runoff, Reynolds Creek watershed, Idaho. *Water Resources Research*, *10*(2), 284–294. <https://doi.org/10.1029/WR010i002p00284>
- Sullivan, P. L., Hynek, S. A., Gu, X., Singha, K., White, T., West, N., et al. (2016). Oxidative dissolution under the channel leads geomorphological evolution at the Shale Hills catchment. *American Journal of Science*, *316*(10), 981–1026. <https://doi.org/10.2475/10.2016.02>
- Tague, C., & Grant, G. E. (2009). Groundwater dynamics mediate low-flow response to global warming in snow-dominated alpine regions. *Water Resources Research*, *45*, W07421. <https://doi.org/10.1029/2008WR007179>
- Tennant, C. J., Harpold, A. A., Lohse, K. A., Godsey, S. E., Crosby, B. T., Larsen, L. G., et al. (2017). Regional sensitivities of seasonal snowpack to elevation, aspect, and vegetation cover in western North America. *Water Resources Research*, *53*, 6908–6926. <https://doi.org/10.1002/2016WR019374>
- Teuling, A. J., Lehner, I., Kirchner, J. W., & Seneviratne, S. I. (2010). Catchments as simple dynamical systems: Experience from a Swiss prealpine catchment. *Water Resources Research*, *46*, W10502. <https://doi.org/10.1029/2009WR008777>
- Tóth, J. (1999). Groundwater as a geologic agent: An overview of the causes, processes, and manifestations. *Hydrogeology Journal*, *7*(1), 1–14. <https://doi.org/10.1007/s100400050176>
- Troch, P. A., Carrillo, G., Sivapalan, M., Wagener, T., & Sawicz, K. (2013). Climate-vegetation-soil interactions and long-term hydrologic partitioning: Signatures of catchment co-evolution. *Hydrology and Earth System Sciences*, *17*(6), 2209–2217. <https://doi.org/10.5194/hess-17-2209-2013>
- Troch, P. A., Lahmers, T., Meira, A., Mukherjee, R., Pedersen, J. W., Roy, T., & Valdés-Pineda, R. (2015). Catchment coevolution: A useful framework for improving predictions of hydrological change? *Water Resources Research*, *51*, 4903–4922. <https://doi.org/10.1002/2015WR017032>

- Tromp-van Meerveld, H. J., & McDonnell, J. J. (2006). Threshold relations in subsurface stormflow: 2. The fill and spill hypothesis. *Water Resources Research*, 42, W02411. <https://doi.org/10.1029/2004WR003800>
- Wagener, T., Sivapalan, M., & McGlynn, B. (2008). Catchment classification and services—Toward a new paradigm for catchment hydrology. In M. G. Anderson (Ed.), *Encyclopedia of hydrological sciences* (pp. 1–12). John Wiley & Sons, Ltd. <https://doi.org/10.1002/0470848944.hsa320>
- Wagener, T., Sivapalan, M., Troch, P., & Woods, R. (2007). Catchment classification and hydrologic similarity. *Geography Compass*, 1(4), 901–931. <https://doi.org/10.1111/j.1749-8198.2007.00039.x>
- Wang, D., & Cai, X. (2010). Recession slope curve analysis under human interferences. *Advances in Water Resources*, 33, 1053–1061. <https://doi.org/10.1016/j.advwatres.2010.06.010>
- Weisman, R. N. (1977). The effect of evapotranspiration on streamflow recession. *Hydrological Sciences Bulletin*, 3(9), 371–377. <https://doi.org/10.1080/02626667709491731>
- White, T., Brantley, S., Banwart, S., Chorover, J., Dietrich, W., Lohse, K., et al. (2015). The role of critical zone observatories in critical zone science. In *Principles and dynamics of the critical zone* (pp. 15–78). Amsterdam, Netherlands: Elsevier. Retrieved from https://books.google.com/books?hl=en&lr=&id=6_mxAwAAQBAJ&oi=fnd&pg=PA15&dq=tim+white+czo&ots=dePEw0QZW-&sig=eq_hpAcl86Qqggj39GFowsVbyQ#v=onepage&q=timwhiteczo&f=false
- Wittenberg, H. (1999). Baseflow recession and recharge as nonlinear storage processes. *Hydrological Processes*, 13(5), 715–726.
- Wlostowski, A., Molotch, N., & Harman, C. (2021). CZO Network water budget data products. *HydroShare*. <https://doi.org/10.4211/hs.29e2ec85770b42c881ef0750696463e5>
- Woods, R. A. (2009). Analytical model of seasonal climate impacts on snow hydrology: Continuous snowpacks. *Advances in Water Resources*, 32, 1465–1481. <https://doi.org/10.1016/j.advwatres.2009.06.011>
- Yoshida, T., & Troch, P. A. (2016). Coevolution of volcanic catchments in Japan. *Hydrology and Earth System Sciences*, 20, 1133–1150. <https://doi.org/10.5194/hess-20-1133-2016>
- Zapata-Rios, X., Brooks, P. D., Troch, P. A., McIntosh, J., & Guo, Q. (2016). Influence of terrain aspect on water partitioning, vegetation structure and vegetation greening in high-elevation catchments in northern New Mexico. *Ecohydrology*, 9(5), 782–795. <https://doi.org/10.1002/eco.1674>
- Zimmer, M. A., & McGlynn, B. L. (2017). Ephemeral and intermittent runoff generation processes in a low relief, highly weathered catchment. *Water Resources Research*, 53, 7055–7077. <https://doi.org/10.1002/2016WR019742>